Time-lapse seismic inversion for CO_2 saturation with SeisCO2Net: An application to Frio-II site

Zi Xian Leong [a,1,*], Tieyuan Zhu [a,b], Alexander Y. Sun [c]

[a] *Department of Geosciences, The Pennsylvania State University, University Park, PA, USA*
[b] *EMS Energy Institute, The Pennsylvania State University, University Park, PA, USA*
[c] *Bureau of Economic Geology, Jackson School of Geosciences, The University of Texas at Austin, Austin, TX, USA*

ARTICLE INFO

ABSTRACT

Seismic monitoring of geological CO_2 storage (GCS) involves highly nonlinear seismic inversion and petrophysical inversion, making it challenging to estimate CO_2 volume efficiently and detect possible early CO_2 leakages. Deep learning (DL) using convolutional neural networks (CNNs) has shown promise in solving highly nonlinear seismic inversion problems. However, direct estimation of CO_2 plume extent/saturation from time-lapse seismic gathers using DL is still underexplored, with no reported field applications to date. The investigation of field data is primarily hindered by scarcity of field data for neural network training. Other obstacles include highly nonlinear seismic-petrophysics inverse relationship, and presence of noise in field seismic data. We introduce SeisCO2Net, a deep CNN that predicts CO_2 saturation maps directly from time-lapse full waveform shot gathers. For training, we use site-specific geological information, fluid flow physics, rock physics, and seismic modeling to generate synthetic datasets that closely resemble the CO_2 storage site. Synthetic tests show promising results, inspiring us to apply SeisCO2Net's trained weights on field data collected at Frio-II GCS site by leveraging transfer learning principles. As reference, we compare SeisCO2Net's predicted CO_2 saturation maps with results obtained from physics-based inversion. Our analyses show both methods display similar CO_2 plume shapes, reasonable CO_2 plume characteristics, and comparable saturation values. Our results suggest pre-training CNNs on physics-informed synthetic datasets and then applying the learned weights to field data is a viable approach to estimating field CO_2 saturation. This method effectively addresses the scarcity of field training data, thus encouraging the feasibility of long-term GCS monitoring.

1. Introduction

Carbon capture and storage (CCS) technology has been widely recognized as a geoengineering measure for mitigating global CO_2 emissions at gigaton scales (IPCC, 2022). In geological carbon storage, carbon dioxide (CO_2) is typically injected into deep geologic formations (~800 m or deeper) such that it stays under supercritical conditions (Smit et al., 2014). To ensure stable long-term storage, it is preferable to store CO_2 in reservoirs that are bounded by impermeable seals (e.g., depleted oil and gas reservoirs). Nevertheless, proper monitoring, verification, and accounting (MVA) protocols of CO_2 storage are necessary to ensure public safety and regulatory compliance by detecting and quantifying the fate of injected CO_2 plumes and potential leakage from the injection zone.

When CO_2 is injected into a host formation (e.g., a brine aquifer), the displacement of the formation brine by CO_2 would cause a reduction in the fluid bulk modulus and rock bulk density, which in turn alters the physical characteristics (velocities and attenuation) of seismic waves. The response of the rock acoustic velocities to water/gas phase saturation changes and the underlying mechanisms have been studied extensively in the past (White, 1975; Mavko et al., 2009). Significant reductions in compressional wave (P-wave) velocities caused by CO_2 injection into porous sandstones have been reported (Nur and Wang, 1989; Xue et al., 2009) and generally agree with standard rock physics theories. This phenomenon can provide a basis for detecting injected CO_2 fluids by using seismic modeling of P-velocity changes to map the location and movement of subsurface CO_2.

In time-lapse seismic monitoring, seismic sources are continuously

---

* Corresponding author.
  E-mail address: zxnleong@gmail.com (Z.X. Leong).
[1] Currently at Chevron Technical Center, a division of Chevron U.S.A. Inc.

shot over certain time intervals. The difference between pre- and post-CO_2 injection recorded seismic data, or time-lapse seismic data, contains corresponding seismic wave changes (e.g., phase and amplitude) resulting from the change in rock properties (e.g., P-velocity). As a result, time-lapse seismic monitoring has been used in various sites to image CO_2 plume dynamics over time (Harris et al., 1996; Arts et al., 2003; Cole et al., 2022; Chadwick et al., 2004; Lumley et al., 2008; Meadows, 2008; Lüth et al., 2011; Daley et al., 2011; White, 2013, Zhu et al., 2019; Roche et al., 2021). As an example, Chadwick et al. (2004) used time-lapse 3D seismic migrated data (sometimes referred as 4D) collected from Sleipner CCS project to interpret the extent of injected CO_2 plume in the Utsira Sand aquifer. Seismic data obtained via time-lapse manner captures the effects of injected CO_2, bringing insights about the presence, movement, and permanence of the sequestered CO_2 plume, and more importantly the amount of sequestered CO_2 (volume) within the geologic formation.

Conventionally, the estimation of CO_2 saturation (volume) is achieved through a physics-based inversion process that involves multi-stage forward modeling procedures, with the objective of matching a parameter of interest between synthetic and field data. Cole et al. (2022) put forward an inversion scheme to estimate CO_2 saturation and pressure from time-lapse seismic data and tested on data collected at Schiehallion field. In the case of Sleipner CCS project, van der Meer et al. (2000) used reservoir properties (e.g., permeability) derived from wireline logs (gamma rays and resistivity), CO_2 fluid properties known by storage operators, and reservoir-geologic structure from seismic surveys to carefully construct a reservoir model, which was used to simulate 3D CO_2 saturations at different time steps. Arts et al. (2003) converted this manually curated CO_2 saturation models to seismic velocities (P-wave) using Gassmann fluid substitution equations (Gassmann, 1951), which was further used to simulate synthetic seismic data. Both the synthetic and field time-lapse seismic data were qualitatively compared, and they were deemed to have reasonable match. As for Frio-II site, Daley et al. (2011) introduced an CO_2 saturation iterative inversion scheme for matching the first arrival delay times across all time-lapse windows of synthetic data to that of the field. The inversion procedure is as follows. First, a TOUGH2 (Pruess, 1991) reservoir fluid flow model was developed based on permeability distribution from well logs. TOUGH2 is a multi-physics (fluid and heat flow in porous and fractured media) numerical simulator for reservoir modeling. Second, CO_2 saturation maps along with other reservoir flow states (e.g., brine saturation and pressure) are produced from TOUGH2. Third, the CO_2 saturation maps were converted to seismic velocities using White-Dutta-Serrif rock physics modeling routines (White, 1975; Dutta and Seriff, 1979). Fourth, the seismic velocities were used to forward model the synthetic seismic travel times. The reservoir properties such as the reservoir structure and permeabilities were manually refined, guided by 'expert judgement', to generate synthetic seismic travel times that match those from the field. Fifth, the inverted CO_2 saturation maps were simulated by using the best-refined reservoir model. The final synthetic travel time delays show fairly good trend match across the calendar time but still underestimate the magnitude of time delays. Lastly, seismic wavefields were simulated for qualitative comparison which showed agreement in capturing the abrupt decrease in arrival time but cannot match the magnitude and sudden onset of the wavefield change. In the case of Cranfield, Mississippi site, Ajo-Franklin et al. (2013) manually refined P-wave first arrival picks which were provided by site operator. The authors noted that picking of first arrivals is notably challenging in areas with high levels of noise and attenuation. From the refined picks, an inversion of regularized travel time tomography was employed to estimate the P-wave velocity changes due to CO_2 injection. The estimated velocity model is then compared and verified with sonic logs. The P-wave velocity models are converted to CO_2 saturation using White-Dutta-Serif's rock physics equations. Lastly, the inverted CO_2 saturation values are validated with field readings from Reservoir Saturation Tool (RST) logs. The two saturation measurements

were broadly consistent in a qualitative manner; however, there is some vertical offset most likely due to residual depth errors.

As discussed, the inversion of estimating CO_2 saturation from time-lapse seismic data requires tedious and time-consuming workflows as well as steps that are subjected to human errors. The resulting data match between synthetic and field data may not be sufficiently well due to the highly nonlinear relationship between seismic data and CO_2 saturation, inability of inversion schemes to achieve global convergence, and/or model space has too many parameters to invert for. In seismic monitoring, the highly nonlinear inverse problem and complex inversion methods can result in drawbacks such as the increased computational and labor costs, which may adversely affect the accuracy and reliability of quantitative assessment of sequestered CO_2 plume. Consequently, conventional methods may not have the best ability for continuous, long-term seismic monitoring.

Deep learning (DL) has seen burgeoning applications in solving highly nonlinear inverse problems pertaining to geophysics (Yu and Ma, 2021), such as in seismic inversion (e.g., Araya-polo et al., 2018; Wu and Lin, 2020; Li et al., 2020; Sun et al., 2020; Xiong et al., 2021, Cai et al., 2022). In recent years, there have been several studies utilizing deep learning for petrophysical and seismic inversion to estimate CO_2 related properties. CNNs and other DL algorithms such as long short-term memory (LSTM) have been adapted to predict CO_2 leakages from seismic and petrophysics data. For example, Sinha et al. (2020) compares performances of multilayer perceptron, CNNs, and LSTMs to estimate future pressure values from past pressure and injection properties to detect leakage during CO_2 injection. Zhou et al. (2019) used densely connected CNNs to invert leakage mass values from time-lapse seismic gathers. On mapping CO_2 saturation to petrophysical properties, Wen et al. (2021) adapted CNNs to predict CO_2 saturation maps from permeability maps and injection depth and duration fields. As for predicting CO_2 saturation from seismic properties, Zhong et al. (2020) used a cycle-consistent generative adversarial network (CycleGAN) to predict CO_2 saturation from changes in acoustic impedance. Li et al. (2021) used CNNs to predict P-wave velocity changes (ΔV_p) maps from time-lapse seismic shot gathers. For predicting CO_2 saturation from seismic data in a broader context, Liu and Grana (2020) combined ensemble smoother methods with deep autoencoders to map time-lapse post stack seismic gathers to permeability and porosity maps. Wang et al. (2020) used support vector machines and basic LSTM network to estimate CO_2 saturation level classes from seismic attributes (e.g., time delay, phase rotation) derived from gathers, downhole pressure, and total dissolved solids measurements. Li and Li (2021) used 3D CNNs to estimate probabilities of CO_2 distribution from seismic migrated images at Sleipner site. Liu et al. (2023) used physics-informed neural networks to estimate CO_2 saturation and porosity from seismic stacked sections.

To our knowledge, direct prediction of CO_2 saturation from seismic shot gathers using CNNs has been largely understudied, particularly with field seismic data. In CCS field collected seismic data, the primary challenge is the lack of field data for training. Other issues include bad data quality (e.g., non-repeatability noise), large data preprocessing challenges (e.g., time-consuming for large datasets), and increased nonlinearity caused by bad data quality, as well as limited availability of benchmark models for result comparison. In DL studies pertaining to CO_2 inversion, the synthetic input and output datasets are scalable, meaning that the dimensions can be scaled up/down or set to be the same for ease of training. Previous work by Leong et al. (2022) and Um et al. (2022) showed that straight-forward CNNs (e.g., U-Net by Ronneberger et al., 2015) can be used for CO_2 saturation inversion from synthetic seismic gathers as long as both the input and output datasets are in the same dimensions (i.e., data(x,t), saturation(x,z) are in different domain but have same dimensions). However, in practice, field seismic data and benchmark/target CO_2 saturation models may come in different dimension sizes. For instance, consider the Cranfield CO_2 site models in which the seismic velocity (equivalent to CO_2 saturation) maps are $111 \times 121 \times 61$ and seismic gathers are $22 \times 121 \times 1000$

(Huang and Zhu, 2020). While adjusting dimensions to achieve same shapes (e.g., downsampling, resampling, cropping) may be feasible, it can result in information loss. For example, downsampling CO_2 saturation models to larger spatial sampling might hinder precise identification of CO_2 plume growth. Moreover, accurate evaluation of DL predictions necessitates comparison with existing benchmark models, requiring similar dimensions for both DL predictions and benchmark models to attain accurate assessments.

In this paper, extending the study done by Leong et al. (2022), we introduce SeisCO2Net, an innovative approach for predicting CO_2 saturation maps directly from time-lapse full waveform shot gathers. We showcase its effectiveness by applying it to the intricate Frio-II field data, overcoming the considerable challenges associated with implementing CNNs in field applications. This first-ever CNN field application highlights the significance of our contribution while addressing the limitations faced in previous research. The overarching idea is to simulate synthetic seismic gathers and CO_2 saturation dataset that closely mimic the field settings. Following that, we train the field-informed synthetic datasets using CNNs and ultimately apply onto field data. By coupling the nonlinear inverse mapping capabilities of CNNs with field-informed synthetics, we are essentially bridging the gap between field and synthetic data. This mitigates convergence issues and improves accuracy during inference.

This paper is organized as follows: first, we introduce SeisCO2Net; second, we present the Frio-II CO_2 site along with its field datasets; third, we describe the inversion workflow, along with the process of generating field-informed synthetic datasets (CO_2 saturation maps, P-wave velocity maps, seismic shot gathers); fourth, we describe the preprocessing steps for the shot gathers and CO_2 saturation maps; fifth, we discuss the parameterization of SeisCO2Net, presenting its training workflow as well as validation and testing metrics; Lastly, we compare SeisCO2Net's predicted CO_2 saturation maps with those generated by TOUGH2 following the workflow proposed by Daley et al. (2011).

2. Methodology

In this section, we first introduce SeisCO2Net—a combination of deep CNN and autoencoder designed to directly predict CO_2 saturation from seismic gathers. We then introduce the Frio-II site and examine its field collected seismic gathers, and briefly introduce the TOUGH2 benchmark CO_2 models. Next, we outline the inversion implementation workflow, which incorporates site-specific (Frio-II) geological-geophysical models to generate realistic synthetic datasets closely resembling the Frio-II site. By creating numerous physics-informed synthetic datasets for training, we aim to address the scarcity of training field data. Subsequently, we discuss the preprocessing steps required for synthetic datasets. Lastly, we provide a detailed explanation of the parameterization of SeisCO2Net, and its training and validation process.

2.1. SeisCO2Net: seismic gathers to CO_2 saturation neural network

The architecture of SeisCO2Net (Fig. 1) is a combination of an autoencoder (SeisCO2Net-AE) and a deep CNN (SeisCO2Net-Main) which takes in time-lapse shot gathers as inputs and outputs CO_2 saturation maps directly. The idea behind SeisCO2Net is as follows: first, we train SeisCO2Net-AE which converts the CO_2 saturation maps into latent representational features (encoded S_{CO2}); second, we train SeisCO2Net-Main that accepts channel-stacked shot gathers and outputs equally stacked encoded S_{CO2} maps; third, only at prediction, we use the trained Decoder part of SeisCO2Net-AE to decode the encoded S_{CO2} maps to reconstruct them to its previous dimension for evaluation purposes.

SeisCO2Net introduces the following advantages. The autoencoder part, SeisCO2Net-AE, first compresses CO_2 saturation maps into lower-dimension space (latent space) without losing much information. This significantly increases the room for more training samples. A channel-stacked dataset is formed by sorting and stacking data (seismic gathers and CO_2 saturation) from different monitor time steps (post-injection at certain time) in time ascending order in a new dimension (e.g., for 2D maps this would be the third dimension). By enforcing SeisCO2Net-Main to learn on channel-stacked dataset, it can extract and learn latent features that correspond to the temporal migration of CO_2 plume. Direct prediction from individual (channel = 1) seismic gathers to CO_2 saturation maps is highly nonlinear and challenging. By vertically stacking the data in ascending time order (effectively channel-stacking along the third dimension), we guide the CNN to recognize temporal growth patterns in the CO_2 plume, thereby reducing the problem's nonlinearity and improving the predictability of CO_2 saturation from seismic shot gathers. In practice, field seismic time-lapse gathers collected from CCS sites often contain non-repeatable noise (Lumley, 2010). Nevertheless, CNNs being a powerful solver for inverse problems, are able to learn on high-level representational features that correspond to the CO_2 plume migration (Zhong et al., 2019). SeisCO2Net is specifically designed to recognize and learn from the underlying patterns of CO_2 plume temporal expansion, aiming for accurate CO_2 saturation predictions even when the input data contains non-repeatable noise.

SeisCO2Net-AE, which is an autoencoder, essentially converts the original CO_2 saturation maps into smaller dimensions without losing much information. Encoded S_{CO2} maps allow for quicker training. The rest of the architecture is found in Table 1. Notably, we use strided (stride >1) 2D convolutions to downsample the features, 2D transposed convolutions for upsampling, and ReLU as an activation function. Note that at block C4 (output layer of the encoder) we use the Tanh activation function to force the data range to $(-1,1)$. Seismic shot gathers contain both positive and negative polarities owing to the nature of wave propagation. We take account of this physics by implementing Tanh function. Hence, the encoded S_{CO2} maps have values that range $(-1, 1)$. Once SeisCO2Net is trained, we can use the AE-Decoder to reconstruct encoded S_{CO2} maps back to the original input dimension.
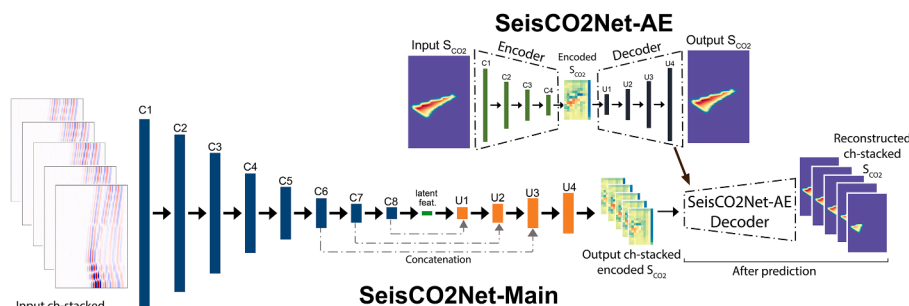
Fig. 1. Full architecture of SeisCO2Net. SeisCO2Net-AE is an autoencoder that compresses CO_2 saturation (S_{CO2}) maps into encoded S_{CO2} maps. SeisCO2Net-Main is a deep CNN with skip layers (concatenation) that inputs channel-stacked shot gathers and outputs encoded S_{CO2} maps. After prediction, we use SeisCO2Net-AE Decoder to reconstruct encoded S_{CO2} maps to the original dimension.

Table 1

Summary of SeisCO2Net-AE architecture. Note the output of AE-Encoder is the encoded S_{CO2}, which is used as the output for SeisCO2Net during its training. After SeisCO2Net-Main prediction, we use AE-Decoder to reconstruct encoded S_{CO2} maps back to the original input dimension.

Architecture	Name	Block	Layers
SeisCO2Net-AE	AE-Encoder	C1	Conv2d + Conv2d + ReLU
		C2	Conv2d + Conv2d + ReLU
		C3	Conv2d + Conv2d + ReLU
		C4	Conv2d + Conv2d + Tanh
	AE-Decoder	U1	ConvTranspose2d + Conv2d + ReLU
		U2	ConvTranspose2d + Conv2d + ReLU
		U3	ConvTranspose2d + Conv2d + ReLU
		U4	Conv2d

SeisCO2Net-Main directly accepts shot gathers and outputs encoded S_{CO2} maps. The convolution channel consists of shot gathers and CO_2 saturation maps that are channel-stacked in time ascending order (sequentially). The rest of the architecture is depicted in Table 2. Similar to the autoencoder, we use strided (stride >1) 2D convolutions to downsample the features, 2D transposed convolutions for upsampling. Following every convolution layer is a Tanh activation function. Inspired by the U-net design (Ronneberger et al., 2015), one important part in our architecture is the implementation of skip connections (concatenations) from blocks C6 to U3 (as shown in Fig. 1). While designing our architecture through trial and error, we find these concatenated skip connections immensely improve the neural network generalization capabilities and prediction accuracies. Concatenated skip connections are known to prevent the gradient vanishing problem and are evident in our task (Huang et al., 2017). They basically mitigate the loss of information by reinforcing the flow of feature information from the encoder (C1 – C8) to the decoder (U1 – U4).

2.2. Field dataset

To lay the groundwork for discussing SeisCO2Net's implementation and inversion workflow, it is essential to first describe the target field dataset, which will better guide readers to understand the proposed effort. We first describe the Frio-II CO_2 injection site and its seismic gather preprocessing steps. Next, we briefly describe the TOUGH2 benchmark CO_2 saturation maps.

2.2.1. Frio-II CO_2 site and seismic gather preprocessing

The Frio-II pilot experiment of CO_2 injection was conducted in September of 2006, where approximately 300 tons of supercritical CO_2 were injected into the Frio "Blue" sandstone reservoir, which is located east of Houston, Texas, USA. The "Blue" reservoir is a thick (~17 m), lithologically heterogeneous Oligocene fluvial sandstone. This reservoir layer is highly porous (~34%), has high permeability (3 – 4 darcy),

Table 2

Summary of SeisCO2Net-Main. Note the output of U4 is encoded S_{CO2} maps. We pass these maps to SeisCO2Net-AE-Decoder to reconstruct them to the original dimensions.

Architecture	Block	Layers
SeisCO2Net-Main	C1	Conv2d + Tanh
	C2	Conv2d + Tanh
	C3	Conv2d + Tanh
	C4	Conv2d + Tanh
	C5	Conv2d + Tanh
	C6	Conv2d + Tanh
	C7	Conv2d + Tanh
	C8	Conv2d + Tanh
	U1	ConvTranspose2d + Tanh
	U2	ConvTranspose2d + Tanh
	U3	ConvTranspose2d + Tanh
	U4	ConvTranspose2d + Conv2d + Tanh

dipping (11 – 15 °), with numerous overlying shale seals (Hovorka et al., 2006). This project is part of the Frio Brine Pilot Experiment to test the feasibility of using CCS technologies in deep subsurface geologic formations to combat the rising anthropogenic CO_2 in the atmosphere. In the Frio-II test, two wells include an injection well and an observation well, where both wells are about 30 m apart (Fig. 2).

At the injection well, there is a fixed piezoelectric source which is located at the top of the reservoir and placed above the CO_2 injector. The source was originally pulsed at four times per second. The continuous active-source seismic data was collected for about 24 h before and 74 h during injection of supercritical CO_2. To improve the signal-to-noise ratio (SNR), the seismic data gathers were generated from extensively stacking 7200 individual pulse recordings, with each gather representing 30 mins stacked data. For baseline monitoring, while 48 gathers could theoretically be collected over 24 h, a single gather was used due to negligible variation among all potential baseline gathers, indicating no significant changes before CO_2 injection. Regarding the available monitoring data, there are 88 seismic gathers over 47.5 h of CO_2 injection, resulting in a total of 89 seismic gathers including the baseline. The stacked pulses are essentially full waveform seismic responses as seismic waves propagate through the rock to receivers in the observation well. Apart from direct P-waves, there are reflected P- and S-waves, and scattered coda waves as the source wavelet interacts with the reservoir formation boundaries and local heterogeneities induced by the CO_2 injection. At the injector, supercritical CO_2 is injected over 5 days at a rate of 1–2 kg/s and continuous seismic source pulses are emitted in which seismic waves travel through the saturated rock to arrive at the observation well. The observation well was originally equipped with 24 hydrophone seismic sensors molded into a multiconductor cable (Daley et al., 2007). Hydrophones sensors were used for higher-frequency response (~ 1 kHz) which is appropriate for the expected spectrum of the piezoelectric source. Despite the sensor protectors, several sensors failed during installation or had degraded signal quality, leaving 13 functional monitoring sensors.

As for the data availability, there are 89 time-lapse seismic gathers (including baseline) which corresponds to total of 47.5 h since the start of CO_2 injection with a few missing time steps in between. The baseline gather is the gather acquired before injection, which is useful to compute time-lapse gathers by subtracting it from subsequent seismic gathers.

As our primary goal is to generate synthetic datasets that closely mimic the field settings, we examine and preprocess the Frio-II field shot gathers. Since we are interested in time-lapse imaging of the CO_2 plume,
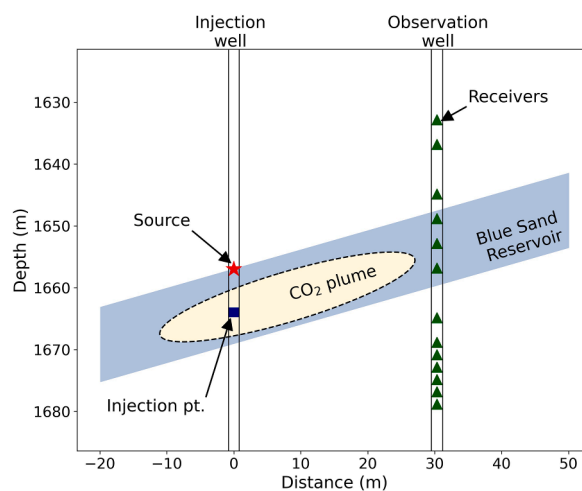
Fig. 2. Schematic of Frio-II CO_2 sequestration site. The thickness of "Blue" reservoir is approximately 17 m thick, dipping at 11 – 15 °. There were originally 24 receivers, however only use 13 receivers (as displayed) are functional well.

we compute the time-lapse gathers (e.g., Fig. 3c) by taking the difference between monitoring (e.g., Fig. 3b) and baseline gathers (e.g., Fig. 3a). Next, we crop the field data to 1600-time steps. To curb the noise levels, we apply a bandpass filter of 250 – 650 Hz to remove higher frequencies which we assume are noise. The final dimensions of the shot gathers are 13×1600. After preprocessing the field data, we design a source wavelet from field dataset by extracting four first-arrival wavelets of four different traces from the baseline shot gather. We choose these four wavelets as they best represent the first arriving wavelet based on visual inspection. We note that the middle traces (1669 m and 1771 m) have the largest amplitudes possibly due to the receivers being closest to the injection point. Next, we align, sum up and average the individual wavelets to produce a final wavelet for generating forward shot gathers. By designing a source wavelet based on field data and instead of a synthetic wavelet, we incorporate more field information into the synthetic shot gathers. This enables the neural network to better learn the features of Frio-II field data, which would be highly beneficial when applying the trained weights onto Frio-II shot gathers.

We note that even after subtracting the pre-injection gather and applying bandpass filter, the time-lapse shot gather (e.g., Fig. 3c) still shows significant amount of non-repeatable noise; most likely contributed by the inability to perfectly repeat the imaging experiment (Lumley, 2010).

2.2.2. TOUGH2 benchmark CO_2 saturation maps

The TOUGH2 saturation maps are computed by careful manipulation of fluid flow, rock physics, and geophysical simulation modeling parameters to generate synthetic travel times to match that of the Frio-II field data. They have dimensions of 467×434, along with a spatial sampling of 0.15 m in both axes.

2.3. SeisCO2Net inversion workflow overview

We introduce a mind map (Fig. 4) that aptly summarizes the overall SeisCO2Net inversion workflow. As with every CO_2 storage site, it starts with a geological model which we denote as background geology model. Using the background geology model, we can obtain prior knowledge about the CO_2 storage site such as reservoir petrophysical properties (e. g., permeability and porosity ranges) and seismic survey information (e. g., source-receiver geometry). This prior knowledge can be utilized to generate realistic synthetic datasets, such as CO_2 saturation maps from fluid flow modeling, P-wave velocity from rock physics modeling, and shot gathers from seismic forward modeling. In addition, generating numerous datasets for training essentially benefits the training of a neural network. All that is left is to use SeisCO2Net to map the relationship between seismic data and CO_2 saturation maps. Incorporating field geological-geophysical information in SeisCO2Net (details
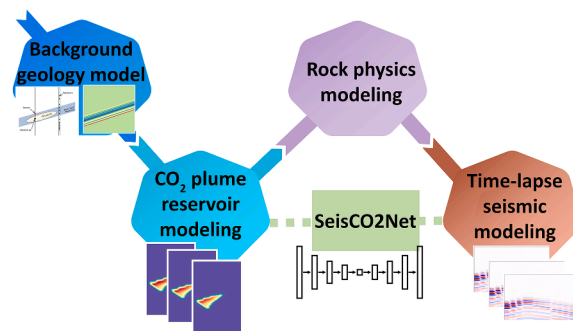

Fig. 4. A mind map summarizing the generation of CO_2 saturation maps and seismic shot gathers that pertains to a certain geological site. To create realistic synthetics, we use prior knowledge about the reservoir (e.g., petrophysical property ranges, source-receive geometry) to simulate CO_2 saturation maps, velocity models, and seismic shot gathers. SeisCO2Net maps the relationship between CO_2 saturation maps and shot gathers.

discussed in next section) can promote better neural network generalization, and hence yielding accurate predictions on Frio-II field data. Additionally, the ability of neural networks to solve inverse problems at great efficiency during inference makes DL-guided methods desirable for long-term seismic monitoring projects.

2.3.1. Frio-II background P-wave velocity model

CO_2 saturation has highly nonlinear relationship with seismic responses owing to the complex physics (fluid flow dynamics, seismic wave propagation, and rock physics interaction) within a rock. Hence, having a geology-informed understanding of the carbon storage site greatly benefits long term seismic monitoring because time-lapse imaging involves repeated acquisition of seismic gathers at later time. The underlying geologic model will not change by much over time, and only the regions that are substituted by supercritical CO_2 induce a change in seismic response. As such, we use Frio-II baseline P-wave velocity model (Fig. 5) as the background geologic model for subsequent seismic velocity changes to be patch on. The baseline P-velocity is derived from 2D extrapolation of logs acquired in the injection well with a local dip determined from gamma rays (Huang and Zhu, 2020). The velocity model had a grid size of 467 (nx) $\times$ 434 (nz) and with grid spacing of 0.15 m for both dimensions.

2.3.2. Reservoir modeling for generating CO_2 saturation maps

In principle, the larger the number of training samples, the easier the neural networks can achieve convergence in establishing complex mappings between their input and output. Hence, we leverage existing information about Frio-II reservoir parameters to synthetically generate
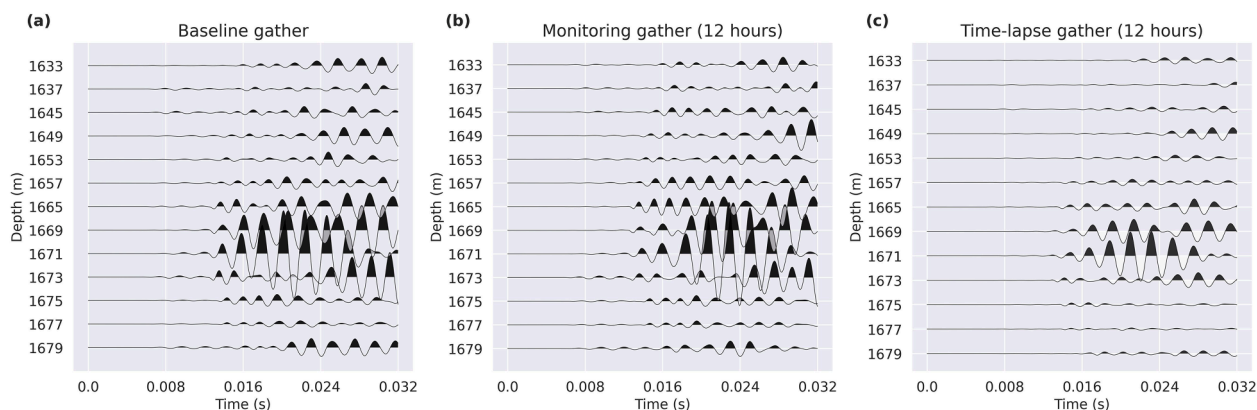

Fig. 3. (a) shows the baseline shot gather collected at Frio-II CO_2 site. (b) is the monitoring gather collected at 12 h post-injection. (c) is the corresponding time-lapse gather (monitoring minus baseline). All these gathers are bandpassed at 250 – 650 Hz.
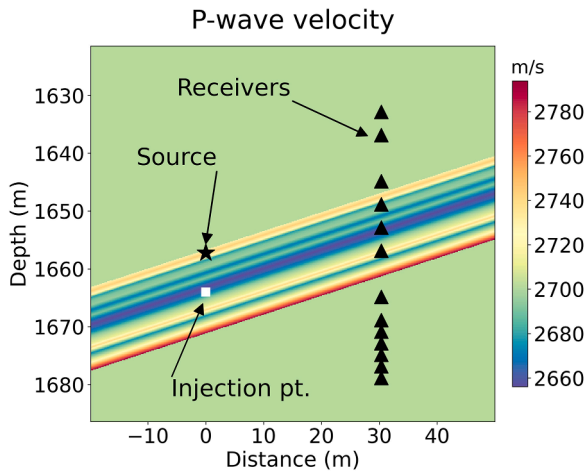
P-wave velocity

Fig. 5. P-wave velocity model from Daley et al. (2011) which acts as the base geologic model for seismic modeling.

numerous CO_2 saturation maps from multiple reservoir realizations. Here, we refer reservoir realizations as permeability and porosity maps. Both maps are inputs for fluid flow reservoir simulation software to generate CO_2 saturation maps.

We use PyGSLIB software, an open-source geostatistical software, to compute reservoir realizations through its sequential gaussian simulation (SGSIM) module (https://opengeostat.github.io/pygslib). In order to generate a randomized permeability or porosity map, SGSIM considers a set of scattered data points and a variogram model which describes the spatial correlation between the sampled data points. SGSIM then stochastically estimates a realization map (e.g., permeability) that best describes the spatial variability of the sampled data points. Our plan is as follows: we generate stochastic realizations of permeability maps and derive porosity values from permeability. Due to computational limitations of the fluid flow reservoir simulation software, we use a larger grid spacing (1.5 m) for both dimensions, resulting in grid sizes of 48 (nx) × 45 (nz). Next, we generate 40 random points scattered over an array of the grid size. For each data point, we assign a random permeability value based on truncated normal distribution with mean (μ) 700 mD and standard deviation (σ) of 1500 mD, as well as lower bound of 250 mD and upper bound of 4000 mD. We chose those parameter values because the resulting distribution can sufficiently encapsulate the permeability ranges of the Frio-II models by Daley et al. (2011). Furthermore, we use different azimuths for different variogram models. Such azimuthal variation increases the diversity of reservoir realization which benefits the generalization capabilities of a neural network.

From the resulting permeability map realizations, we add seals of 10 mD above and below the reservoir. The porosity is assumed to be linearly correlated with log permeability:

$$\varnothing = 0.063(\log k + 1.3) + 0.02, \tag{1}$$

where k represents permeability and $\varnothing$ is porosity. Like permeability, we add seals of $\varnothing = 0.05$ above and below the reservoir. Incorporating the site's geological information in the reservoir realizations (permeability and porosity maps) is effective in providing better constrains in the neural network's learning, hence promoting convergence.

The CO_2 flow simulations are computed via MATLAB Reservoir Simulation Toolbox (MRST) (Lie et al., 2012). MRST is a 3D sequential solver of Darcy's equation for (in)compressible and immiscible flow that utilizes fully-implicit methods based on automatic differentiation routines. We use the co2lab module within MRST to simulate sequestered CO_2 fluid flow movements in the reservoir. As MRST takes in 3D models, we extend our 2D permeability and porosity maps into three-dimensional volumes by replicating the 2D maps in the third dimension. We design the CO_2 saturation simulation workflow based on

template codes provided in the basic 3D two-phase water and gas system simulation (basic_3D_example.m) within MRST-co2lab module. Next, we use the default settings of CO_2 fluid properties as provided in the code template. The reference pressure is set to 15 MPa, reference temperature is at 343.15 K, and brine viscosity is at 8×10^4 Pa/s. At this pressure and temperature, the CO_2 behave as a supercritical fluid as it is above the critical pressure (7.38 MPa) and critical temperature (304.13 K). The injection rate is set to 1 kg/s which is comparable to the 1–2 kg/s used in Frio-II experiment. To match the field setting, we set the time step sampling rate to three hours with five days of total simulation time. The injection point location is determined from the Frio-II site experiment.

The MRST-co2lab simulation outputs CO_2 saturation and pressure 3D volumes. In all the 3D volume outputs, we take the middle 2D slice as the final desired output because we are interested in mapping seismic shot-gathers to 2D CO_2 saturation maps. We upsample both the pressure and CO_2 saturation maps using linear interpolation to match the dimension of the Frio-II velocity model (Fig. 5). Due to the MRST-co2lab generated CO_2 saturation maps having smaller grid size (48 × 45) (we avoid using larger dimensions due to computational limitations), upsampling the maps to the original dimension (467 × 434) results in exaggerated CO_2 plume size, particularly in the vertical component. To solve this issue, we use a modified spatial sampling of dx = 0.15 m and dz = 0.25 m during linear interpolation. Next, we apply small amounts of geometrical adjustment such as translational shifting and rotations to fit the CO_2 plume in the reservoir. Lastly, we pad the resulting maps with zeros so that the final CO_2 saturation maps have the same dimension as the Frio-II velocity model (467 × 434). Although these artificial geometrical adjustments introduce some inaccuracies in the fluid flow physics, this workaround ensures the CO_2 plume contain within the reservoir. Most importantly, the supercritical CO_2 fluid flow dynamics (e.g., plume migration pattern and CO_2 saturation) across different time steps and reservoir realizations are retained.

The pressure maps are retained for the conversion of CO_2 saturation maps to P-wave velocity models as pressure information is required by rock physics modeling to compute the fluid bulk modulus as part of Gassmann fluid substitution.

2.3.3. Rock physics modeling to estimate P-wave velocity

The implementation of our rock physics modeling largely follows the approach outlined by Zhong et al. (2020). CO_2 saturation maps need to be converted to seismic velocities (in this case P-wave velocity) so that seismic shot gathers can be simulated via seismic forward modeling. The replacement of brine with supercritical CO_2 changes how rocks behave under stress, effectively changing the rock's bulk modulus. Gassmann fluid substitution theory established a relation for which when a rock is loaded under an increment of compression, such as from a passing seismic wave, an increment of pore-pressure change is induced, which resists the compression and therefore stiffens the rock (Mavko et al., 2009; Gassmann, 1951; Biot, 1956a,b). Gassmann fluid substitution relationship is as follows, to estimate the bulk modulus after saturation (K_{sat}),

$$K_{sat} = K_{dry} + \frac{\left(1 - \frac{K_{dry}}{K_{matrix}}\right)^2}{\frac{\varnothing}{K_{fl}} + \frac{1 - \varnothing}{K_{matrix}} - \frac{K_{dry}}{K_{matrix}^2}}, \tag{2}$$

where K_{dry} is the bulk modulus before CO_2 injection, K_{matrix} is the bulk modulus of mineral making up the rock, K_f is the bulk modulus of the pore fluid, and $\varnothing$ denotes the porosity. We obtain K_{dry} by referring to Pride (2005)'s model in which,

$$K_{dry} = K_{matrix} \frac{1 - \varnothing}{1 + c\varnothing}, \tag{3}$$

where c is the consolidation parameter that characterizes the degree of

consolidation between the grains within the rock. Depending on the degree of cementation, one can expect the approximate range $2 < c < 20$, for consolidated sandstones, where 2 being extremely consolidated and 20 poorly consolidated (Pride, 2005). In essence, the larger the c, the 'looser' the rock matrix is. We assume c to be 15 as Frio-II "Blue" reservoir is highly permeable. We compute K_{matrix} by taking the Voigt-Reuss-Hill average (Hill, 1952), which is useful to estimate the effective elastic moduli of a rock, is denoted by,

$$K_{matrix} = \frac{M_{Voigt} + M_{Reuss}}{2},$$ (4)

where M_{Voigt} is also known as the Voigt upper bound (Voigt, 1928), and M_{Reuss} is the Reuss lower bound (Reuss, 1929), in which they are defined by,

$$M_{Voigt} = \sum_{i=1}^{N} f_i M_i,$$ (5)

$$\frac{1}{M_{Reuss}} = \sum_{i=1}^{N} \frac{f_i}{M_i},$$ (6)

where f_i is the volume fraction of the mineral constituent i within the rock, and M_i is the bulk modulus of the mineral constituent i. The injected fluids consist of two components: CO_2 and brine. To compute the bulk modulus of the CO_2-brine mixture, K_{fl}, we refer to Wood's average relation (Wood and Lindsay, 1956),

$$K_{fl} = \left[\frac{S_{brine}}{K_{brine}} + \frac{S_{CO_2}}{K_{CO_2}} \right]^{-1}$$ (7)

where S_{brine} and S_{CO_2} are the gas saturations for brine and CO_2, and K_{brine} and K_{CO_2} are the corresponding bulk moduli of brine and CO_2. S_{brine} and S_{CO_2} are generated during reservoir modeling (see previous section). We refer to Batzle and Wang (1992) relations to compute the bulk modulus of brine (K_{brine}) and CO_2 (K_{CO_2}) as they are a function of pressure, temperature, salinity (for fluids) and specific gravity (for gas). For this study, we use the open-source rock physics modeling package (https://github.com/sconten/rppy) to compute K_{brine} and K_{CO_2}. For more information, Kumar (2006) provides detailed and concise derivations of Batzle and Wang (1992) relations. Finally, the P-wave seismic velocity, V_p, can be calculated by,

$$V_p = \frac{\sqrt{K_{sat} + \frac{4\mu}{3}}}{\rho_b}$$ (8)

where K_{sat} is the bulk modulus of the rock after saturation, μ is the shear rock modulus, and ρ_b is the bulk rock density after saturation. It is important to note that the shear modulus stays the same even after fluid substitution (Biot, 1956a,b; Berryman and Milton, 1991). For our study, bulk density (ρ_b) consists of two parts, solid rock density (ρ_m) and effective fluid density (ρ_f), which can be obtained by the following equation,

$$\rho_b = \varnothing(S_{brine}\rho_{brine} + S_{CO_2}\rho_{CO_2}) + (1 - \varnothing)\rho_{matrix}$$ (9)

where rock matrix density (ρ_{matrix}) can be calculated by summing up the volume fractions (f_i) of mineral constituents i within the rock,

$$\rho_{matrix} = \sum_{i=1}^{N} f_{m_i} \rho_{m_i}$$ (10)

where ρ_{m_i} is the mineral density. As for the Frio-II, we assume the reservoir storage layer contains mineral fractions that represent a typical sandstone, which is ideal for CO_2 sequestration. The values of fractions, bulk modulus, mineral constituents can be found in Table 3.

Table 3
List of bulk moduli, densities, reservoir fractions of rock minerals used in this study.

Mineral	Bulk modulus, M_i (GPa)	Density, ρ_{m_i} (g/cm³),	Reservoir fractions, f_{m_i}
Feldspar	75.6	2.63	0.2
Quartz	36.6	2.65	0.7
Rock fragments	80	2.7	0.1

2.3.4. Frio-II synthetic seismic gathers and CO_2 saturation maps preprocessing

From the P-wave velocity models and extracted field wavelet, we use viscoacoustic forward modeling to simulate seismic data. Viscoacoustic physics contains attenuation dynamics, and will better mimic the field settings as attenuation is significant from field measurements from seismic CO_2 monitoring datasets (e.g., Zhu et al., 2017). For the attenuation quality factor (Q), we set the background geology as 1000, the reservoir as 50, and injected CO_2 fluid as 25. These Q values are based on the typical values of sandstone and CO_2 saturated sandstone (e.g., Steeples, 2005). The source and receivers' geometry are extracted from Frio-II field settings (e.g., Fig. 2), source frequency at 800 Hz, time sampling rate (dt) is 2e-5 s and spatial sampling (dx and dz) is 0.15 m. We use Xing and Zhu (2019)'s viscoacoustic seismic modeling framework to simulate seismic shot gathers. We assume the seals (Anahuac shale) above and bottom the reservoir are homogeneous (2,700 m/s) and have similar P-velocity, as depicted in Fig. 5. This assumption simplifies our analysis by focusing solely on the seismic response attributable to the CO_2 plume. Therefore, even if the seals or adjacent strata are stratified, time-lapse seismic analysis will only show changes specifically induced by the plume, independent of the surrounding geological complexities.

We provide an overview of data processing steps in Fig. 6. There are inherent differences between field data and synthetic data due to the nature of the former. The Frio-II field seismic gathers have significant non-repeatable noise, meaning the recorded seismic response at every subsequent time step seemingly contain new variation of noise. This predominantly affects time-lapse shot gathers as noise artifacts will remain even after subtraction of baseline shot gather, as evident in Fig. 4c. Since we perform synthetic forward modeling, the time-lapse shot gathers are naturally free from noise. Furthermore, the field data coda waves have relatively higher amplitudes than that of synthetic. To resolve this field-synthetic mismatch, we bridge the gap by performing the following preprocessing steps on synthetic shot gathers:

1) applying similar preprocessing steps that is used on Frio-II field data, i.e., bandpass and cropping,
2) adding small amount of time-gain on the synthetics,
3) normalizing each shot gather by its absolute maximum value, and
4) constraining SeisCO2Net to accept sequentially channel-stacked data.

For CO_2 saturation maps, we only take account of the regions traveled by seismic waves emanating from the source and receivers (e.g., Fig. 2). As such, we apply these preprocessing steps:

1) apply a triangle mask (Fig. 6b) such that only the region that is covered by the seismic ray path is retained (mask value of 1); whereas the rest of the area is left out (mask value of 0),
2) crop the maps to an intermediate dimension of 300×200 in accordance with the Frio-II source-receiver geometry.

As a final note, the preprocessed shot gathers and CO_2 saturation maps have dimensions of 13×1600 and 300×200, respectively.

(a) Seismic gathers

(b) CO₂ sat. maps

(c) Sequential stack for SeisCo2Net
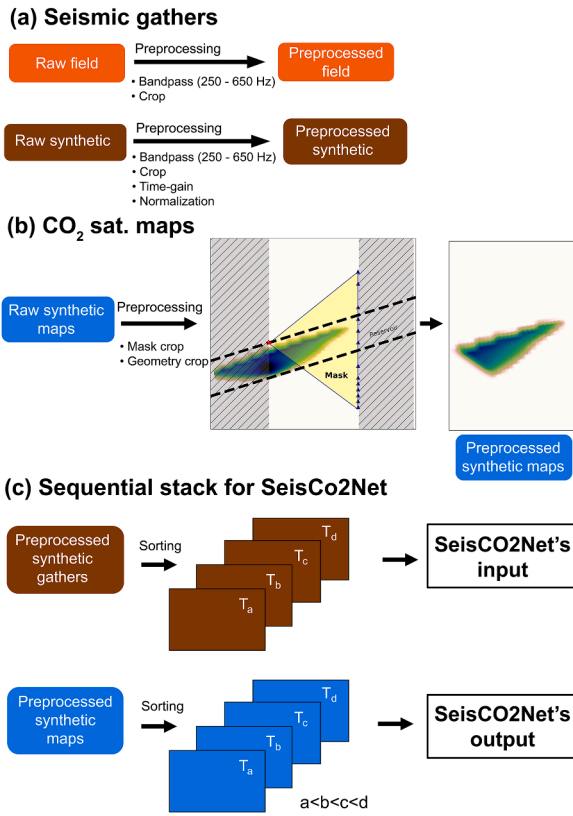
Fig. 6. Data preprocessing workflow. We start from (a) in which we bandpass and crop the field gathers. Next, we apply the same bandpass (250 – 650 Hz) to the synthetic gathers, along with small amounts of time-gain, and normalization. In (b), the triangular mask (yellow) highlights the areas of seismic ray paths. We use this mask to isolate the CO_2 plume, ensuring that only the relevant portions (as displayed) within the ray paths are retained. Then, we crop out the regions bounded by the injection and observation well to produce preprocessed synthetic maps (300 × 200). Subsequently in (c), we channel-stack the gathers-maps in sequential order. For example, {T_1, T_3, T_6, T_9, …, T_N}; where $N = 10$. The shot gathers and CO_2 maps will be served as Seis-CO2Net's input and output, respectively.

2.4. Parameterization of SeisCO2Net

We tailor the network's architecture to the dimensions of the pre-processed dataset. Table 4 summarizes the input and output shapes of every convolution block in SeisCO2Net. There are 372,820 total trainable parameters. This approach intends to minimize alterations to the original data dimensions, thereby avoiding potential artifacts that could arise from resampling or reshaping. Such a strategy allows for a direct and rigorous comparison with benchmark models, and preserves the resolution necessary for a detailed analysis of CO_2 plume behavior.

2.5. Training workflow

CNNs randomly initialize their weights and biases according to a predefined statistical distribution, with kernels at every Conv2d layer sampling input data accordingly. In our case, we use the default setting which is Xavier distribution (Glorot and Bengio, 2010). This means we can estimate the neural network's statistical uncertainties by running numerous iterations of training. From the variation of weights, we can compute the mean prediction as the desired final prediction, and standard deviations as prediction uncertainties.

SeisCO2Net training procedure can be summarized as follows:

1) Train SeisCO2Net-AE to produce encoded S_{CO2} maps,

Table 4
Summarizes the input and output array shapes of SeisCO2Net. The dimensions in the input and output shapes are denoted by channel × nx × nz.

Architecture	Name	Block	Input shape	Output shape
SeisCO2Net-AE	AE-Encoder	C1	1 × 300 × 200	8 × 60 × 40
		C2	8 × 60 × 40	16 × 30 × 20
		C3	16 × 30 × 20	32 × 15 × 10
		C4	32 × 15 × 10	1 × 15 × 10
	AE-Decoder	U1	1 × 15 × 10	32 × 30 × 20
		U2	32 × 30 × 20	16 × 60 × 40
		U3	16 × 60 × 40	8 × 300 × 200
		U4	1 × 300 × 200	8 × 60 × 40
SeisCO2Net-Main		C1	10 × 13 × 1600	2 × 15 × 320
		C2	2 × 15 × 320	4 × 15 × 64
		C3	4 × 15 × 64	8 × 15 × 32
		C4	8 × 15 × 32	16 × 8 × 16
		C5	16 × 8 × 16	32 × 8 × 8
		C6	32 × 8 × 8	64 × 4 × 4
		C7	64 × 4 × 4	64 × 2 × 2
		C8	64 × 2 × 2	64 × 1 × 1
		U1	64 × 1 × 1	64 × 2 × 2
		U2	64 × 2 × 2	64 × 4 × 4
		U3	64 × 4 × 4	32 × 8 × 8
		U4	32 × 8 × 8	10 × 15 × 10

2) Train SeisCO2Net-Main where input is time-lapse shot gathers and output is encoded S_{CO2} maps,

3) Repeat 20 times to obtain 20 variations of trained weights. We assume that 20 varied weights can sufficiently provide a distribution of weights that could estimate the prediction's uncertainties.

4) Compute average of 20 predictions as final prediction and standard deviations from 20 predictions as uncertainties.

2.6. Training loss function and evaluation metric

For both SeisCO2Net-Main and SeisCO2Net-AE, we use mean-square-error (MSE) as the training loss function due to CO_2 saturation maps containing CO_2 plume growth that varies spatially and ranges from 0.0 (no saturation) to 1.0 (completely saturated).

As discussed, only after prediction, we use the SeisCO2Net-AE Decoder to reconstruct the predicted encoded S_{CO2} maps (e.g., 15 × 10) back to its intermediate dimension (e.g., 300 × 200). For accuracy metric, we use $CO2Accuracy = 1 - \frac{MSE_{pred}}{MSE_{blank}}$; where MSE_{pred} is the MSE between prediction and the ground truth; MSE_{blank} is the MSE between the corresponding ground truth and an array of zeros. The array of zeros represents no saturation. CO2Accuracy ranges from 0.0 to 1.0; where 0.0 (0%) means the predictions are completely dissimilar while 1.0 (100%) means predictions are completely similar to the ground truth.

3. Results

This section is split into four parts. First, we discuss the results of synthetic dataset (e.g., CO_2 saturation and seismic gathers) generated from the Methodology. Second, we discuss the SeisCO2Net training, validation, and testing results on the synthetic dataset. Third, we evaluate predictions of the trained SeisCO2Net on testing dataset with added noise. Lastly, we show the results of applying the trained SeisCO2Net on field Frio-II seismic gathers.

3.1. Synthetic seismic gather and CO₂ saturation maps generation

We generate 40 reservoir realizations (permeability-porosity maps) based on 40 different variogram azimuths. These different azimuths vary over 360°, starting from 0° with uniform 9° sampling step for each realization. Fig. 7 shows four examples of these realizations. Each of these four reservoir realizations are based on different variogram azimuths. For example, note how the orientation of permeability "clumps"

Permeability
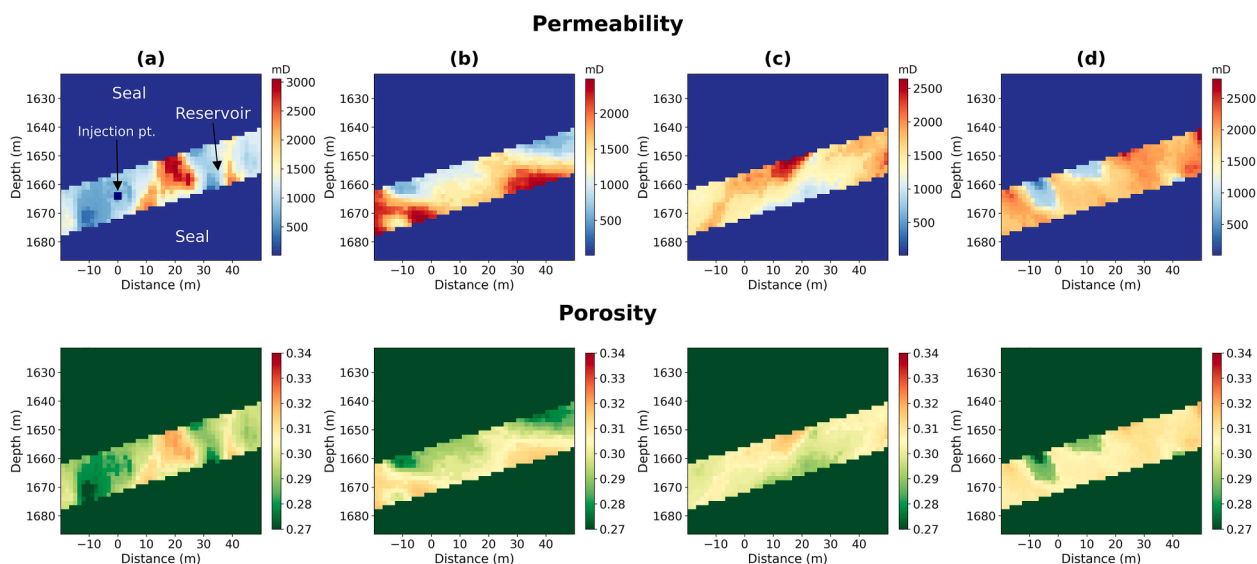
Porosity

Fig. 7. Top row has four examples of permeability realizations; bottom row shows corresponding porosity realizations. Permeability maps are generated using SGSIM. Each of the reservoir realization has different variogram azimuths. For example, (a), (b), (c), and (d) have 0°, 9°, 18°, and 27° azimuth, respectively. In total, we generate 40 reservoir realizations.

with similar values are different across the four realizations. This encourages injected CO_2 to permeate through the reservoir differently for different realizations. As such, by generating numerous realizations with different variogram azimuths, we are increasing the diversity of dataset.

For each reservoir realization, we use MRST (with parameter settings as discussed in Section 2.3.2) to simulate CO_2 saturation maps. We match the sampling rate of TOUGH2 benchmark CO_2 saturation models at a three-hour interval. From the resulting CO_2 saturation maps, we only retain the maps starting from 6 h to 63 h post-injection because the plumes prior to that do not exhibit significant changes. In summary, each reservoir realization has 20 CO_2 saturation maps. Fig. 8 shows two examples of synthetic CO_2 saturation maps. Note how the buoyant supercritical CO_2 migrates updip towards the right end of the reservoir. The two examples are from two distinct reservoir realizations, generated from dissimilar permeability and porosity maps. Due to the reservoir characteristics being different, the CO_2 fluid flow exhibits different flow behavior. For example, at a specific time step (e.g., 48 h), the migration of CO_2 plume varies depending on the permeability maps used. Besides, the migration of the CO_2 plume varies across time steps. The varied fluid flow patterns serve to boost the variance of CO_2 saturation map training samples which encourage the neural network to achieve greater

generalization capabilities.

From the CO_2 saturation maps, we estimate absolute P-wave velocities using Gassmann fluid substitution equations (discussed in Section 2.3.3). Figs. 9d – 9f show the time-lapse Frio-II P-velocity model while the baseline model is shown in Fig. 5. Next, we simulate shot-gathers (Figs. 9j – 9l) based on the P-wave velocities and attenuation (Figs. 9g – 9i). As discussed before, we perform preprocessing (refer to Section 2.3.4) on the shot gathers and CO_2 saturation maps to prepare for SeisCO2Net.

In summary, for each 40 reservoir realizations, we generate and select 20 CO_2 saturation and corresponding shot gathers. Data leakage occurs when parts of the validation and/or testing dataset are included in the training dataset, leading to artificially inflated performance during testing. This practice is incorrect as it hinders proper evaluation of the generalization capabilities of a neural network. To combat this, we first randomly split 36 reservoir realizations for training, two realizations for validation, and two realizations for testing. Next, we create channel-stacked datasets (reasons of which are discussed in Section 2.1) by computing 10 combinations of different time steps for each reservoir realization. The computation of all 10 combinations from 20 possibilities (20C10 = ~184k) is excessively large, thus infeasible for
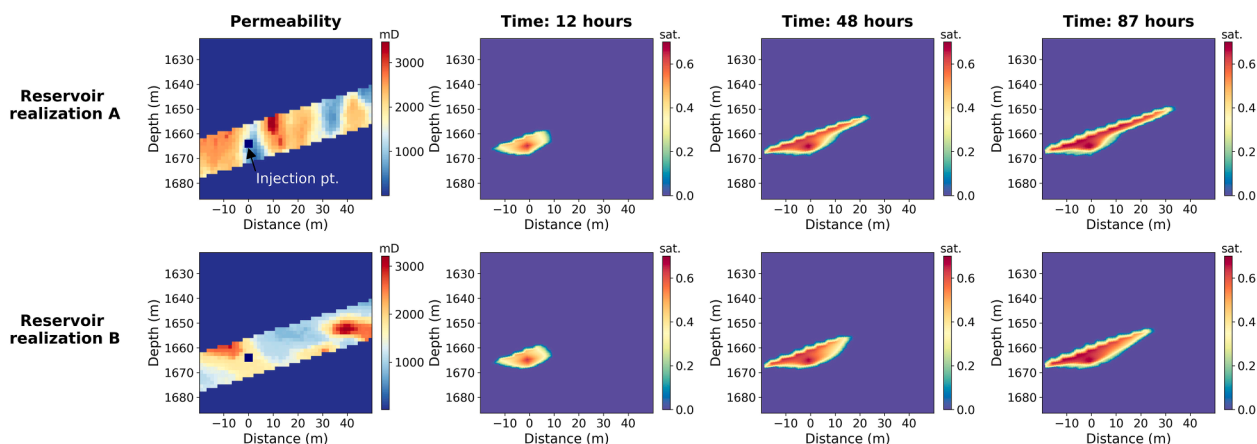
Fig. 8. The top row depicts reservoir realization A, while the bottom row shows reservoir realization B. These two examples illustrate how different reservoir realizations can result in varying CO_2 plumes across different time steps.
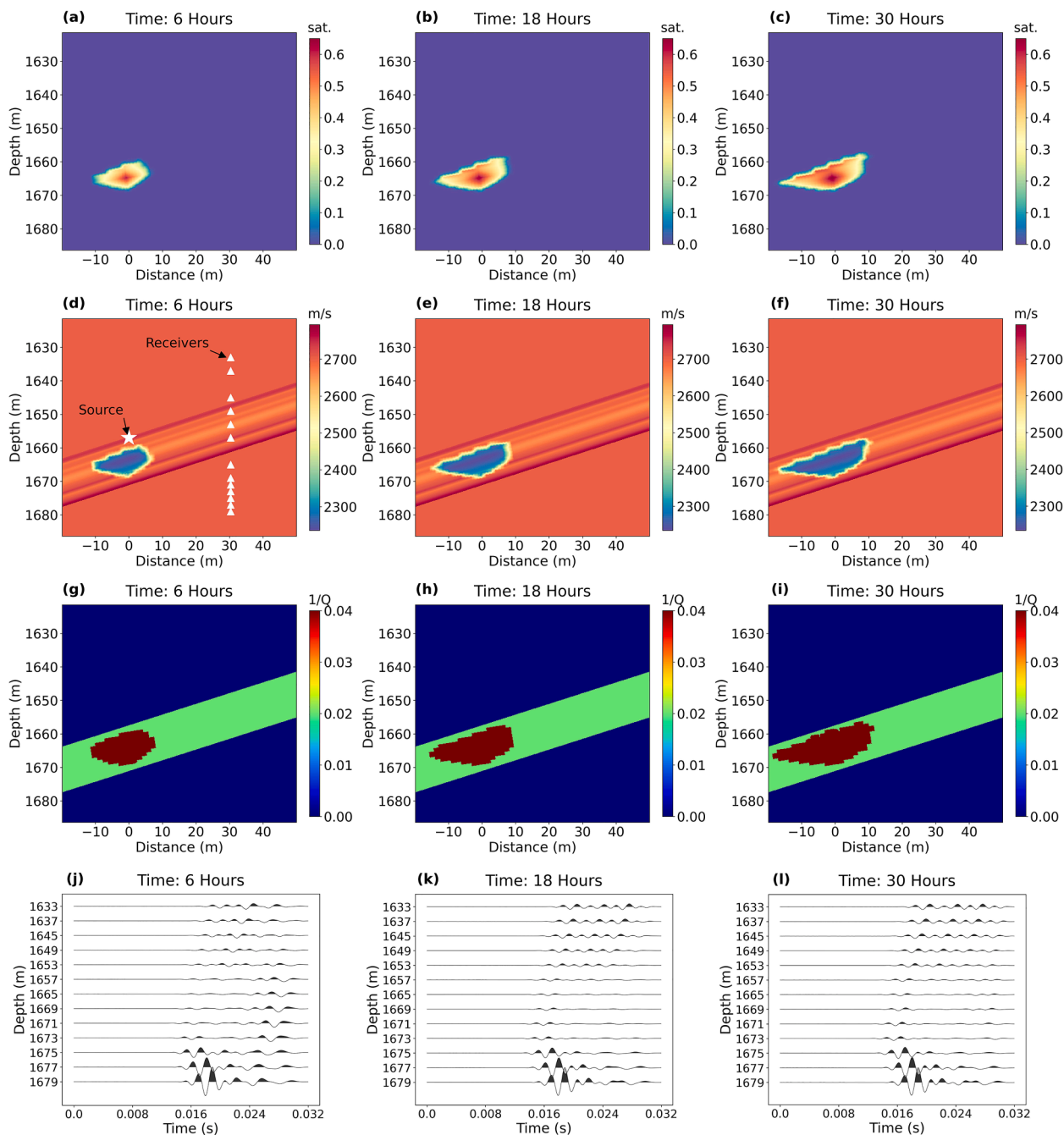
Fig. 9. (a)-(c) are synthetic CO_2 saturation maps in three elapsed times. (d)-(f) shows the corresponding V_p models after Gassmann fluid substitution from the CO_2 saturation maps. (g)-(i) are the attenuation Q used for seismic modeling. (j)-(l) depicts simulated viscoacoustic shot gathers.

SeisCO2Net training. Instead, for each reservoir realization, we randomly select 300 combinations out of the ~184k combinations for the training dataset. We sort the time steps in ascending time order. For example, an example of combination would be {T1, T2, T3, T5, T7, T8, T12, T14, T16, T18}. We repeat these steps for validation and testing dataset but at 500 combinations for each reservoir realization. Now, the training dataset has 10,800 (36 reservoir realizations × 300 combinations) samples, validation, and testing dataset both have 1000 (2 reservoir realizations × 500 combinations). Nevertheless, we quickly realize our GPU (NVIDIA RTX 2080 Ti 10 GB RAM) is overwhelmed by the immense number of datasets. Therefore, we further reduce the training dataset to 5193 samples and 400 samples for validation dataset, both by random selection. The testing dataset remains the same at 1000 samples. Fig. 10 shows one example of preprocessed training dataset –

shot gather and corresponding CO_2 saturation. This example is considered as one sample because all the 10 shot gathers and CO_2 saturation are channel-stacked.

3.2. SeisCO2Net: training, validation, and testing

We use the following hyperparameters for SeisCO2Net-AE: batch size of 40, Adam optimizer, learning rate of 0.001, and 500 epochs. We save only the weights with the lowest training loss to ensure convergence. At the end of training (Fig. 11a), SeisCO2Net-AE achieves a low MSE of 6.5e-6. We show the training loss in logarithmic scale to better illustrate the training progress. The autoencoder training proves to be smooth and achieved convergence rapidly, indicating SeisCO2Net-AE's ability to encode CO_2 saturation maps effectively.
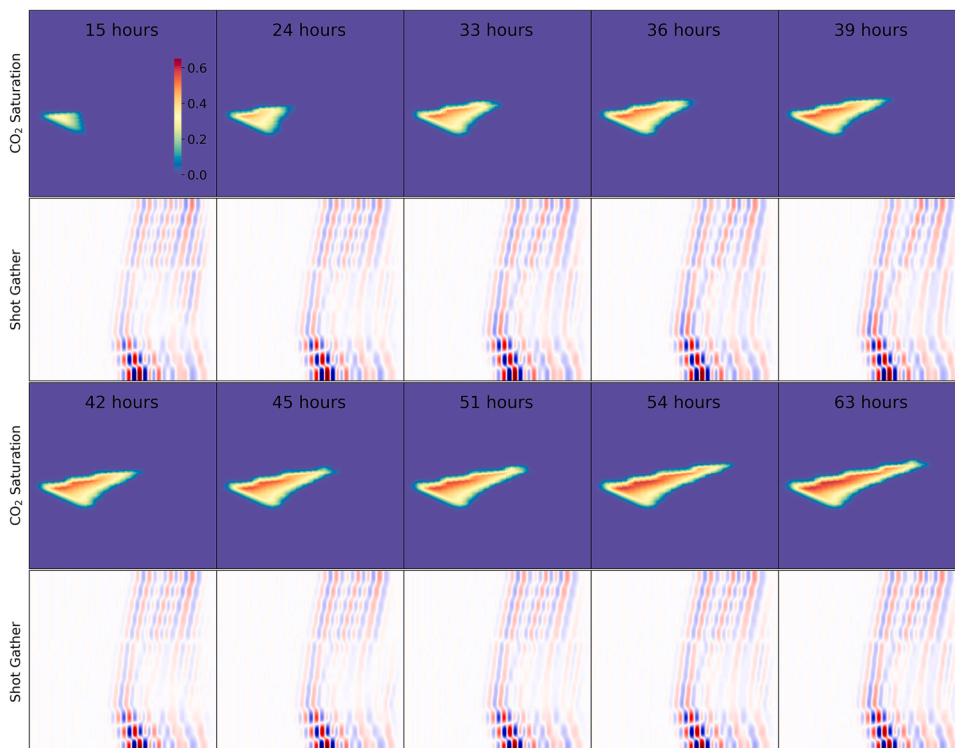
Fig. 10. Example of one preprocessed training dataset. Each dataset includes 10 random combinations of time steps. In this example, we show a combination of {15, 24, 33, 36, 39, 42, 45, 51, 54, 63} hours of post-injection monitoring dataset. The seismic gathers and CO_2 saturation are channel-stacked in the third dimension. As for the dimensions, SeisCO2Net inputs seismic gathers of $10 \times 13 \times 1600$, and outputs CO_2 saturation maps of $10 \times 300 \times 200$.
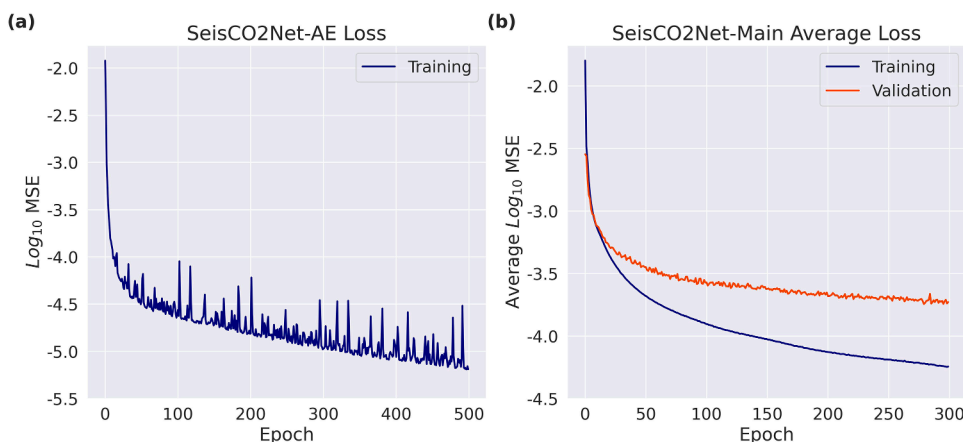

Fig. 11. (a) shows the training loss progress of SeisCO2Net -AE. (b) shows the average loss of SeisCO2Net-Main from 20 trained weights. Both losses are presented on a logarithmic scale to better illustrate the progression of training. The model's performance on validation dataset closely follows that of training dataset. There are 5193 training dataset and 400 validation dataset.

As for SeisCO2Net-Main, the training hyperparameters are as follows: batch size of 40, learning rate of 0.001, 300 epochs, and Adam optimizer. We let SeisCO2Net-Main train for 20 iterations, and at every iteration, we retain the best weights based on lowest validation loss. SeisCO2Net requires a total of 48 h for training, with each weight taking around 2 h. Once we obtain 20 iterations of trained weights, we compute the average MSE to gauge the training progress (Fig. 11b). From the variation of weights, we can compute the mean prediction as the desired final prediction. We also compute the standard deviation of the predictions. These uncertainties give us an estimate on the robustness of SeisCO2Net's predictions. We note not only the training loss curve is smooth but also the validation loss. The average validation loss closely follows the training loss, indicating that SeisCO2Net-Main achieved

great generalization capabilities.

To further examine the validation dataset (400 samples) accuracy, we use the SeisCO2Net-AE Decoder to reconstruct the predicted encoded S_{CO2} maps (15×10 dimension) back to its original intermediate dimension of 300×200. The average CO2Accuracy on the reconstructed validation dataset is 99.71%. As for the performance on testing dataset, the reconstructed testing dataset (1000 samples) has CO2Accuracy of 99.23%. Fig. 12 shows an example of prediction on testing dataset.

The immediate prediction of SeisCO2Net-Main is encoded S_{CO2} (Fig. 12a), a high-level representation of CO_2 saturation maps in the latent space. We note that the encoded S_{CO2} map roughly resembles a downsampled ground truth map (Fig. 12c). The reconstructed prediction
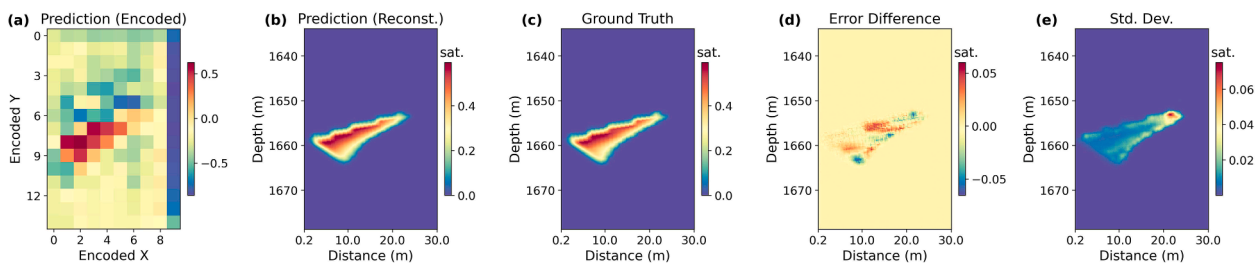
Fig. 12. (a) the average prediction (dimension of 15 × 10) of SeisCO2Net-Main from 20 trained weights. (b) the reconstructed CO_2 saturation map from using SeisCO2Net-Decoder (dimension of 300 × 200). (c) is the ground truth. (d) shows the subtraction of (b) from (c). (e) shows the corresponding uncertainties (standard deviation) from the trained weights.

(Fig. 12b) is generated by applying SeisCO2Net -AE Decoder on the encoded S_{CO2} map (Fig. 12a). We note the error difference (Fig. 12d) between the reconstructed predictions and ground truth is generally minimal at the regions close to the injection point. The error increases with the extent of plume growth. For example, at the farthest extent of the plume (tip), the error seems to be higher. This phenomenon is supported by the uncertainty map (Fig. 12e) where the standard deviation is the highest at the tip of plume growth. In terms of seismic inversion, this aligns with the physics as the farthest extent or edge of the plume growth oftentimes have the smallest plume size and thus resulting in the highest uncertainties.

We further examine the robustness of the CO_2 saturation prediction by comparing its predicted forward data and the original synthetic gather (Fig. 13). Based on our excellent CO2Accuracy results, in our results, we note the waveforms closely match and overlap even in most parts of the coda waves. This indicates the trained SeisCO2Net is successful in achieving convergence and implies that the forward and inverse problem is complete.

3.3. Testing on synthetic noisy dataset

We further evaluate the trained SeisCO2Net on the similar testing dataset but with band limited (100 – 1000 Hz) gaussian noise added to the seismic gathers. Furthermore, we adjust the level of noise to concentrate at the middle portion of traces to replicate the strong noise signals in Frio-II field gathers (e.g., Fig. 3c). The average CO2Accuracy is 94%. In Fig. 14, we show two examples of predictions on the noisy dataset. It is evident that the noisy shot gathers (Figs. 14a and 14e, in red) contains noisy waveforms in the later arrivals. In theory, the presence of these noisy waveforms would introduce errors to SeisCO2Net's predictions. The predictions (Figs. 14b and 14f) show some visible differences of the CO_2 saturation to corresponding ground truth (Figs. 14c
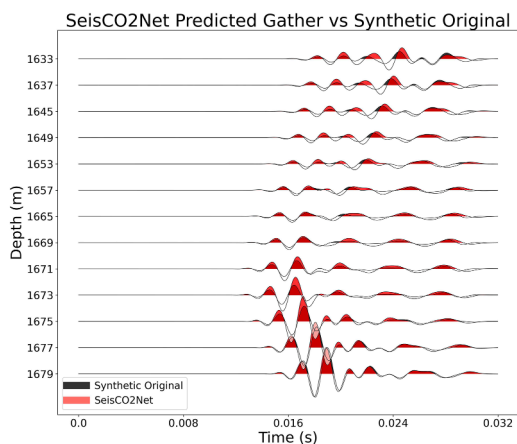
and 14g). The direct differences are shown in Fig. 14d and 14h. The CO2Accuracy in these examples is 98% respectively. Nevertheless, the predicted CO_2 plume shape and plume extent at monitor time exhibit considerable similarity to the ground truth.

Based on the testing results, SeisCO2Net demonstrates robust resistance to noise in seismic gathers. This finding underscores SeisCO2Net's capability in learning features associated with CO_2 plume growth, even in the presence of significant noise. Overall, the robust performance on the testing dataset also emphasizes SeisCO2Net's semi-supervised learning capability.
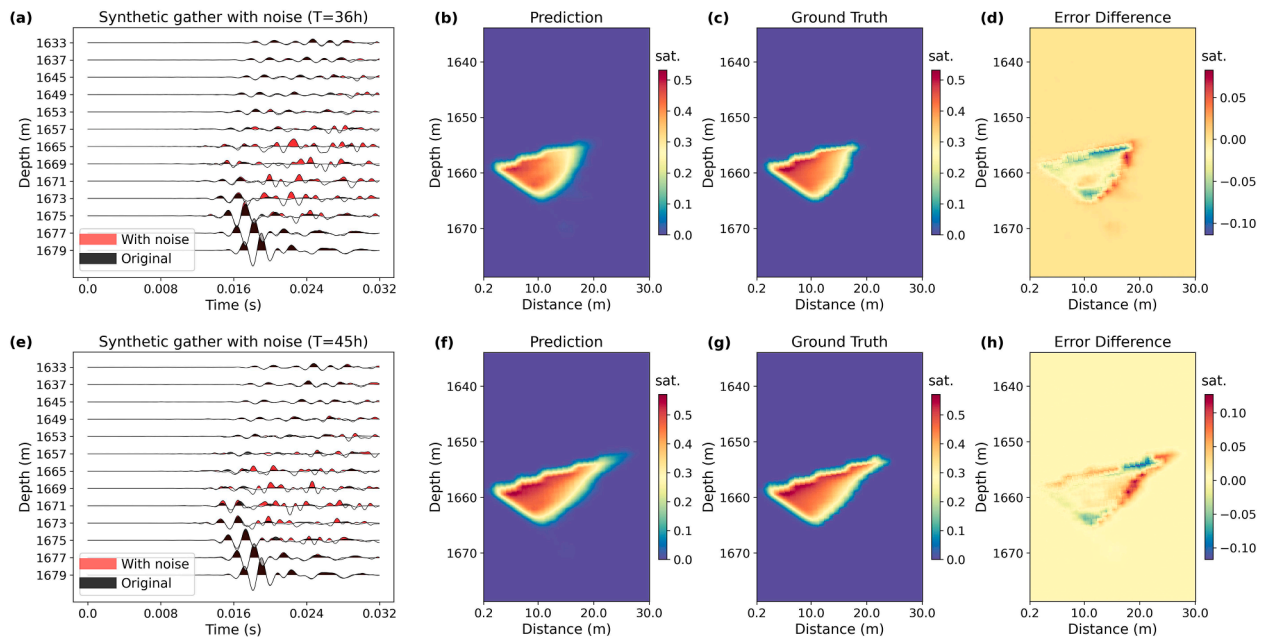
3.4. Applications to Frio-II field shot gathers

As discussed before, the availability of field shot gather data is limited to 47.5 h post injection. We exclude time-lapse data of 39-hours post-injection, as these time-lapse gathers do not exhibit significant plume growth.

After applying the 20 trained weights to the preprocessed field gathers, we pad the predictions with zeros to reconstruct them back to the original dimension of 467 × 434, which allows us to directly compare our results with the CO_2 saturation maps predicted by the TOUGH2 model from Daley et al. (2011). We show the comparison of SeisCO2Net predictions (Figs. 15a – 15c) and TOUGH2 models (Figs. 15d – 15f) as well as the prediction uncertainties (Figs. 15g – 15i) from the 20 trained weights. Visual examination of SeisCO2Net inverted CO_2 saturation maps indicates that the CNN performs favorably in comparison to the physics-based TOUGH2 models, particularly in terms of CO_2 plume shape predictions. While SeisCO2Net's predicted CO_2 saturations show slightly lower values, they generally fall within the range predicted by TOUGH2. It is important to recognize that TOUGH2 predictions are also approximations and cannot be considered the absolute ground truth, as there is no single, completely accurate observation. In general, when only comparing CO_2 saturation maps predictions, SeisCO2Net's inversion show similarities in terms of plume shape, CO_2 saturation values, and plume extent when compared to the physics-based TOUGH2 model.

The map of predicted uncertainties show that errors tend to be higher at the middle of the plume. This is reasonable because CO_2 saturations are typically highest at plume's center due to its proximity with the injection point. Moreover, we note that the uncertainty maps indicate slightly larger plume shapes (e.g., Fig. 15h) than the predictions (e.g., Fig. 15b) and generally show greater lateral extent of plume growth. This allows us to assess the risks associated with the spatial extent (boundaries) of plume growth, as well as determine the reliability of predictions. For example, when uncertainties indicate a wider lateral plume extent than predicted, it signals the implementation of more cautious MVA protocols to constrain the plume.

To further gauge the reliability and trustworthiness of our prediction, we apply the same procedure of converting CO_2 saturation maps to velocity models (Equations 2 – 10) and perform forward modeling using similar configurations as discussed in the simulation of Frio-II synthetic shot gathers. We repeat these steps on TOUGH2 CO_2 saturation maps to

Fig. 13. Comparison of forward gather generated from SeisCONet prediction (Fig. 12b) vs. original synthetic gather.

Fig. 14. Two examples of testing the trained SeisCO2Net on seismic gather with noise. Both rows consist of shot gathers from different monitor time, i.e., top row is at $T = 36$ h, bottom row is at $T = 45$ h. (a) and (e) show seismic gathers with noise added (in red) overlaying the original without noise. (b) and (f) show the SeisCO2Net predictions, while (c) and (g) are the respective ground truth. (d) and (h) are the subtractions of predictions from ground truth.

generate TOUGH2 predicted forward data for comparison. The comparison of select SeisCO2Net and TOUGH2 predicted forward data is shown in Fig. 16.

From the data matching, SeisCO2Net's predicted data have comparable data matching performance to that by TOUGH2 models. The individual wavelets in SeisCO2Net's forward synthetic gathers match (Fig. 16a and 16b) the Frio-II field data very well especially at the receivers that record the first waves (e.g., at depth 1669 m and 1671 m). At other traces of depths 1633 – 1653 m, we note that SeisCO2Net's predicted synthetic gather (Fig. 16a and 16b) exhibits favorable match, especially at the first few wavelets, in terms of both wave arrivals and amplitudes. The TOUGH2 forward modeling synthetic data (Fig. 16c and 16d) expectedly match well as it is derived from multi-physics models that match synthetic and field travel times. In summary, both methods demonstrate similar performance in matching the first few wavelets, but fail to match the coda waves.

From the results, we enlarge the shot gather at 36 h post-injection (Fig. 16b) for better visual comparison. Fig. 17 shows the enlarged results. We also compare the data matching, and attach the corresponding CO_2 saturation prediction overlay with Frio-II site schematics for illustration purposes. We highlight the good data match in dark blue dashed circles. We see that at receiver of depth 1645 m, the synthetic coda waves match with the field data significantly well. The first arriving wavelet and the trailing coda wavelets closely overlap the field data. Besides, at receiver of depth 1653 m, the data match also show good matching. At trace of 1669 depth, the first arriving wavelet completely matches the field data. The data match at larger offsets (e.g., depths 1633 m and 1637 m; 1677 m and 1679 m) are generally out of phase. We attribute this discrepancy primarily to two factors: (1) the persistent presence of non-repeatability noise that throughout the experiment, and (2) imperfect CO_2 predictions and/or velocity models leading to significant differences in seismic energy caused by scattered and reflected waves. In general, when comparing this CO_2 saturation map prediction to that of TOUGH2 (Fig. 15f), we observe that both display agreeable plume shapes and CO_2 saturation values. Given these similarities, we posit that the predicted CO_2 plume at 36 h post-injection is likely accurate.

4. Discussion

In this paper, we address the issues of applying the state-of-art neural network algorithm to field time-lapse seismic shot gather data for directly estimating CO_2 saturation by proposing SeisCO2Net. In practice, the main challenges include the lack of training data and presence of non-repeatable noise stemming from time-lapse seismic surveys. We overcome these challenges by allowing SeisCO2Net to train on physics-informed synthetic dataset that closely resembles the field settings. To elaborate further, we use stochastic simulation techniques to generate training samples that resemble Frio-II by using site-specific geology and reservoir information. SeisCO2Net first compresses CO_2 saturation maps to smaller dimensions to alleviate computation burden. Next, we impose constraints on SeisCO2Net by channel-stacking the datasets (seismic gathers and CO_2 saturation maps) in ascending time order, facilitating the learning of latent features related to CO_2 plume growth. This channel-stacking constraint enables SeisCO2Net to yield satisfactory results on Frio-II field data, even in the presence of non-repeatable noise within seismic gathers.

The seismic monitoring system at the Frio-II storage site only consists of a single seismic source, which limits the effectiveness of any conventional seismic inversion and imaging techniques. These methods generally require multiple sources to produce accurate CO_2 saturation estimates, and they fall short when faced with data limitation scenarios, like at Frio-II. Our CNN-based model, SeisCO2Net, however, thrives under such constraints. It successfully performs inversion with limited data, overcoming a challenge that conventional methods cannot. This adaptability also marks CNN-based model's noteworthy advantage over the more sophisticated physics-informed neural network (PINN) and Fourier neural operator (FNO) algorithms, which have been applied to multiphase flow simulations (Wen et al., 2022), seismic waveform modeling (Yang et al., 2023), and multiphysics seismic to CO_2 saturation inversion (Yin et al., 2023). While these models are efficient, they primarily solve partial differential equations that describe the physical processes involved, which can be problematic with limited data or process understanding. In extreme cases with a single seismic source, as with our study, inadequate physical observations and incomplete source-receiver coverage could disable the applications of PINN and

SeisCO2Net Predictions

TOUGH2 Benchmark
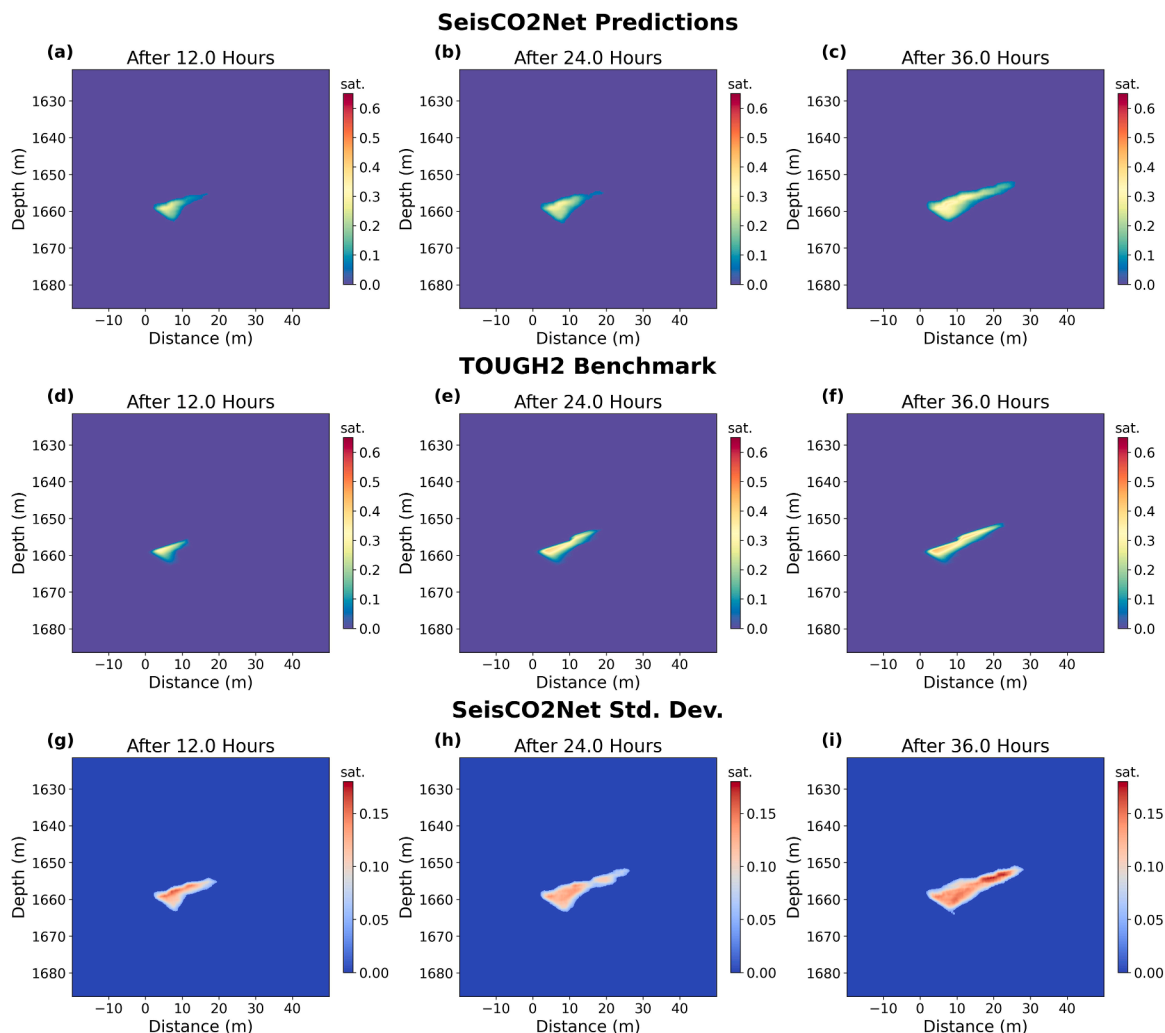
SeisCO2Net Std. Dev.

Fig. 15. (a)-(c): Predicted CO_2 saturation maps on Frio-II field shot gathers at different elapsed times. We compare the predictions with TOUGH2 benchmark models (Daley et al., 2011) in (d)-(f). From the 20 trained weights, we compute SeisCO2Net's uncertainties (g-i).

FNO algorithms. In contrast, CNN-based models, which are purely data-driven, are not constructed to directly incorporate physical laws. Instead, we supplement this by infusing geophysics-informed information into the training dataset, effectively compensating for the absence of explicit physical modeling. This allows us to generate extensive training data that mirrors the conditions of the field, irrespective of whether the data encompasses sufficient observational details such as seismic sources and coverage. The capacity of CNNs to learn the intrinsic mapping between seismic gathers and CO_2 saturation maps from large volumes of training data equips them to sidestep some of the constraints that hamper conventional physics-based approaches. The encouraging outcomes from both synthetic and field data in this study underscore the potential of purely data-driven ML models to transcend some limitations inherent to traditional physics-based methods. These findings illuminate a potential for employing CNNs effectively in scenarios where physics-based models may falter due to data limitations.

To some extent, SeisCO2Net can be modified and adapted to other field sites. SeisCO2Net's input and output convolution kernel and padding sizes can be adjusted to accommodate different field seismic gathers and CO_2 saturation dataset. Although adding more convolution layers can enhance its nonlinear solving capabilities, it may result in reduced efficiency. SeisCO2Net combines autoencoder and deep CNNs, utilizing dimensionality reduction to boost the training and prediction efficiency while minimizing information loss when using encoded CO_2 saturation maps. This strategy underscores its applicability in large field

sites (e.g., Sleipner) requiring higher resolution maps. Given site-specific geological-geophysical information (e.g., reservoir characterization and velocity models), a comprehensive training dataset covering diverse reservoir parameters and seismic responses can be created. By employing advanced deep learning algorithms like SeisCO2Net, CO_2 saturation maps can be efficiently predicted, significantly reducing the need for labor-intensive conventional CO_2 inversion workflows.

As for the general adaptability of SeisCO2Net, we acknowledge that our trained SeisCO2Net model could not be directly applied to other CCS sites. As other CCS sites contain different subsurface geology, seismic source-receiver geometry, and reservoir conditions, the direct application of Frio-II-trained SeisCO2Net to those CCS sites would be infeasible. Nonetheless, the primary use case of CO_2 sequestration sites is to ensure the permanence (e.g., >50 years) of CO2 storage. The long-term use case of CO_2 sequestration outweighs the cons of simulating new synthetic datasets specific to the CO_2 storage site.

There are several assumptions underlying our approach. We assume that there CO_2 storage site has well-characterized information on the reservoir and its surrounding geology. This prior information might be difficult to obtain if the CO_2 is stored in complex and challenging environments such as offshore depleted deep oil and gas reservoirs. Moreover, we note that SeisCO2Net's inference time is only a matter of seconds. The time taken to generate all synthetic datasets (CO_2 saturation maps and seismic gathers) is approximately less than 3 days. The training time for SeisCO2Net is around 48 h, with each trained weight
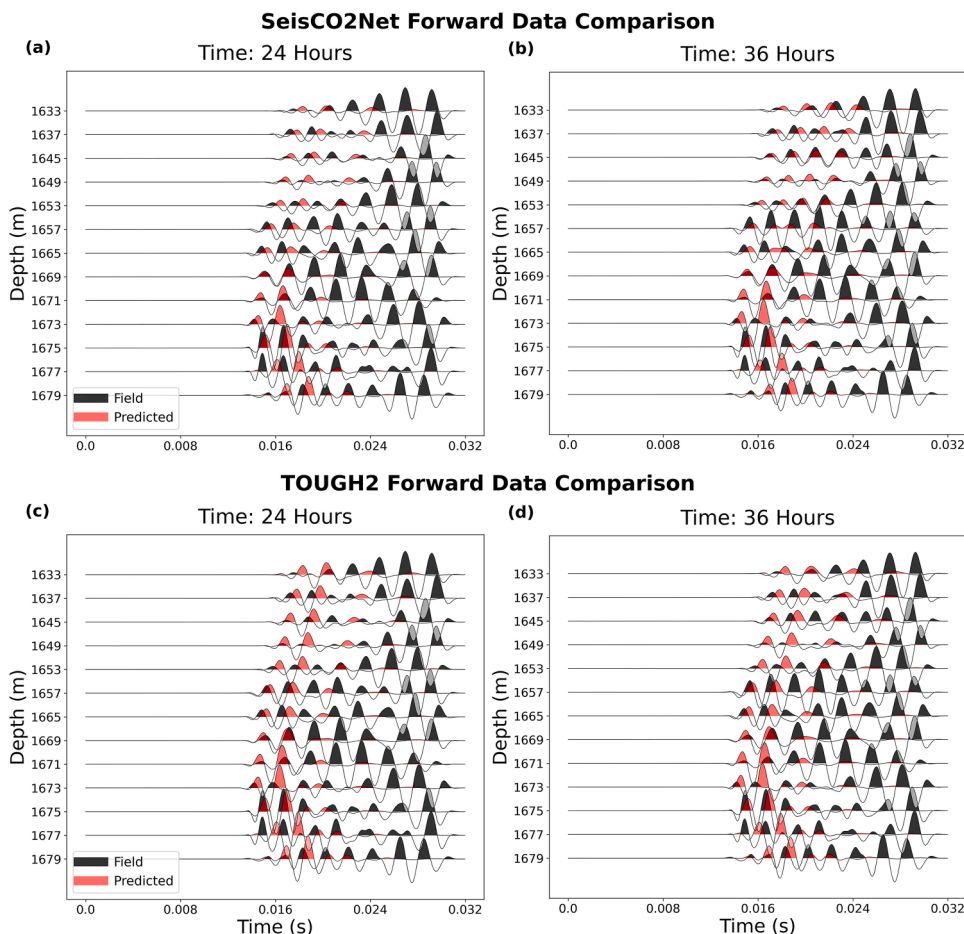
Fig. 16. (a) and (b) present two examples of comparison between the predicted forward data simulated based on SeisCO2Net CO_2 saturation maps' predictions and corresponding Frio-II field gathers. (c) and (d) depict the comparison using physics-based TOUGH2 predictions.
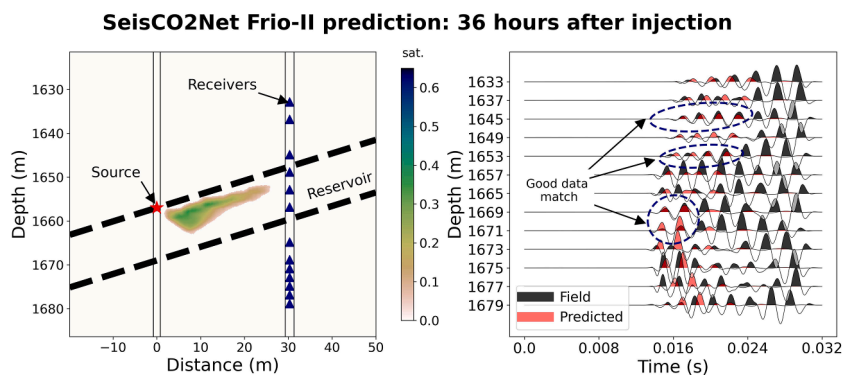

Fig. 17. Here, we depict an enlarged version of Fig. 16b. Left panel shows the corresponding CO_2 saturation map predicted by SeisCO2Net on Frio-II field data 36 h post-injection. Right panel illustrates the comparison of synthetic vs. field data. The dark blue circles highlight several instances where the data matches well, which increases our confidence in the CO_2 plume prediction.

taking approximately 2 h. Despite this, the computational cost is relatively low compared to the potential cost savings in accumulated inference time from long-term seismic monitoring. As discussed earlier, due to GPU RAM limitations (RTX 2080 Ti 10 GB RAM), we randomly select 0.08% (5193) of the total 6.6 million sample possibilities for training. Despite this, SeisCO2Net is able to generalize significantly well (Fig. 10) especially when validated and tested on separate dataset that is not part of training. The validation and testing dataset are created by initially separating the reservoir realizations for training, validation and testing to prevent data leakage. The strong performance of SeisCO2Net

that is trained on a fraction of dataset further validates the nonlinear solving capabilities of CNNs. In retrospect, we recommend utilizing batch loading techniques to accommodate more extensive training datasets. Nonetheless, moving forward, we recommend using an improved GPU with considerably more RAM especially for CCS sites that have large datasets.

Improvements could be made to our workflow. Gassmann equations assume the rock unit to be saturated homogeneously and do not include dynamic pressure effects related to mesoscale heterogeneity in fluid distribution. In the reservoir under more realistic conditions, the CO_2

distribution tends to contain spatial heterogeneity. As such, White-Dutta-Serrif's model for patchy saturation (White, 1975; Dutta and Seriff, 1979) might be more suitable to estimate the velocities. In addition, the forward data generated through viscoacoustic seismic modeling does not fully capture all aspects of all seismic wave physics. Therefore, in practical applications, it would be more precise to use a viscoelastic modeling approach, which accounts for the propagation of shear waves (S-waves). Besides, we note that more noise reduction methods could be done in the field data preprocessing. Methods such as deconvolution and f-k filtering could play important roles to further reduce the noise in the field dataset, which may improve prediction results.

5. Conclusion

Conventional methods for inverting CO_2 saturation from time-lapse seismic data typically consist of tedious and time-consuming workflows, as well as preprocessing steps that are subjected to human error. In this paper, we propose a deep learning (DL) solution, SeisCO2Net, that estimates CO_2 saturation maps directly from time-lapse seismic shot gathers (only one seismic shot). Compared to the existing DL methods, this study is the first to demonstrate the implementation of neural networks (via SeisCO2Net) on field seismic data by training on realistic physics-informed synthetic datasets (CO_2 saturation and shot gathers) that closely mimic field settings. We show a field application example at Frio-II CO_2 sequestration pilot site. Our implementation workflow enables the generation of numerous training dataset which essentially overcomes the paucity related to field training data. The prediction results of SeisCO2Net exhibit a close resemblance to TOUGH2 in terms of CO_2 plume shape and saturation values. This assessment is further supported by the good match between SeisCO2Net's predicted forward data and Frio-II field data, particularly at the first few arriving wavelets. Because of its instantaneous prediction, our proposed SeisCO2Net along with its implementation workflow could potentially pave the way for long-term seismic monitoring of geological CO_2 storage.

Data availability

Frio-II datasets can be obtained at https://edx.netl.doe.gov/dataset/frio-2-raw-cassm-datasets. Codes associated with this research are available upon request.

CRediT authorship contribution statement

Zi Xian Leong: Conceptualization, Methodology, Software, Investigation, Formal analysis, Visualization, Writing – original draft. **Tieyuan Zhu:** Supervision, Resources, Funding acquisition, Writing – review & editing. **Alexander Y. Sun:** Supervision, Writing – review & editing.

Declaration of competing interest

The authors declare that they have no known competing financial interests or personal relationships that could have appeared to influence the work reported in this paper.

Acknowledgements

References

Ajo-Franklin, J.B., Peterson, J., Doetsch, J., Daley, T.M., 2013. High-resolution characterization of a CO2 plume using crosswell seismic tomography: Cranfield, MS, USA. Int. J. Greenhouse Gas Control 18, 497–509. https://doi.org/10.1016/j.ijggc.2012.12.018.

Araya-Polo, M., Jennings, J., Adler, A., Dahlke, T., 2018. Deep-learning tomography. Lead. Edge 37 (1), 58–66. https://doi.org/10.1190/tle37010058.1.

Arts, R., Chadwick, A., Eiken, O., & Zweigel, P. (2003). *Interpretation of the 1999 and 2001 time-lapse seismic data (WP5.4)*. TNO-report NITG 03-064-B.

Batzle, M., Wang, Z., 1992. Seismic properties of pore fluids. Geophysics 57 (11), 1396–1408. https://doi.org/10.1190/1.1443207.

Berryman, J.G., Milton, G.W., 1991. Exact results for generalized Gassmann's equations in composite porous media with two constituents. Geophysics 56 (12), 1950–1960. https://doi.org/10.1190/1.1443006.

Biot, M.A., 1956a. Theory of propagation of elastic waves in a fluid-saturated porous solid. I. Low-frequency range. J. Acoust. Soc. Am. 28 (2), 168–178. https://doi.org/10.1121/1.1908239.

Biot, M.A., 1956b. Theory of propagation of elastic waves in a fluid-saturated porous solid. II. Higher frequency range. J. Acoust. Soc. Am. 28 (2), 179–191. https://doi.org/10.1121/1.1908241.

Cai, A., Qiu, H., Niu, F., 2022. Semi-supervised surface wave tomography with Wasserstein cycle-consistent Gan: method and application to southern California plate boundary region. J. Geophys. Res.: Solid Earth 127 (3), e2021JB023598. https://doi.org/10.1029/2021JB023598.

Chadwick, R.A., Zweigel, P., Gregersen, U., Kirby, G.A., Holloway, S., Johannessen, P.N., 2004. Geological reservoir characterization of a CO2 storage site: the utsira sand, Sleipner, northern north sea. Energy 29 (9–10), 1371–1381. https://doi.org/10.1016/j.energy.2004.03.071.

Cole, S., Lumley, D., Meadows, M., Tura, A., 2022. Pressure and saturation inversion of 4D seismic data by rock physics forward modeling. In: SEG Technical Program Expanded Abstracts 2002, pp. 2475–2478. https://doi.org/10.1190/1.1817221.

Daley, T.M., Ajo-Franklin, J.B., Doughty, C., 2011. Constraining the reservoir model of an injected CO2 plume with crosswell CASSM at the Frio-II brine pilot. Int. J. Greenhouse Gas Control 5 (4), 1022–1030. https://doi.org/10.1016/j.ijggc.2011.03.002.

Daley, T.M., Solbau, R.D., Ajo-Franklin, J.B., Benson, S.M., 2007. Continuous active-source seismic monitoring of CO2 injection in a brine aquifer. GEOPHYSICS 72 (5), A57–A61. https://doi.org/10.1190/1.2754716.

Dutta, N.C., Seriff, A.J., 1979. On White's model of attenuation in rocks with partial gas saturation. Geophysics 44 (11), 1806–1812. https://doi.org/10.1190/1.1440940.

Gassmann, F., 1951. Elastic waves through a packing of spheres. Geophysics 16 (4), 673–685. https://doi.org/10.1190/1.1437718.

Glorot, X., Bengio, Y., 2010. Understanding the difficulty of training deep feedforward neural networks. In: Proceedings of the Thirteenth International Conference on Artificial Intelligence and Statistics, pp. 249–256.

Harris, J.M., Langan, R.T., Fasnacht, T., Melton, D., Smith, B., Sinton, J., Tan, H., 1996. Experimental verification of seismic monitoring of CO 2 injection in carbonate reservoirs. In: SEG Technical Program Expanded Abstracts 1996, pp. 1870–1872. https://doi.org/10.1190/1.1826505.

Hill, R., 1952. The elastic behaviour of a crystalline aggregate. Proc. Phys. Soc. London Sect. A 65 (5), 349–354. https://doi.org/10.1088/0370-1298/65/5/307.

Hovorka, S.D., Benson, S.M., Doughty, C., Freifeld, B.M., Sakurai, S., Daley, T.M., Kharaka, Y.K., Holtz, M.H., Trautz, R.C., Nance, H.S., Myer, L.R., Knauss, K.G., 2006. Measuring permanence of CO2 storage in saline formations: the Frio experiment. Environ. Geosci. 13 (2), 105–121. https://doi.org/10.1306/eg.11210505011.

Huang, G., Liu, Z., Weinberger, K.Q., 2017. Densely Connected Convolutional Networks. Proceedings of the IEEE Conference on Computer Vision and Pattern Recognition (CVPR) 2261–2269.

Huang, C., Zhu, T., 2020. Towards real-time monitoring: data assimilated time-lapse full waveform inversion for seismic velocity and uncertainty estimation. Geophys. J. Int. 223 (2), 811–824. https://doi.org/10.1093/gji/ggaa337.

IPCC, 2022. Climate Change 2022: Mitigation of Climate Change: Contribution of Working Group III to the Sixth Assessment Report of the Intergovernmental Panel on Climate Change. Cambridge University Press.

Kumar, D., 2006. A tutorial on Gassmann fluid substitution: formulation, algorithm and Matlab code. Geohorizons 11, 4–12.

Leong, Z.X., Zhu, T., Sun, A.Y., 2022. Estimating CO2 saturation maps from seismic data using deep convolutional neural networks. In: Second International Meeting for Applied Geoscience & Energy, pp. 510–514. https://doi.org/10.1190/image2022-3746727.1.

Li, B., Li, Y.E., 2021. Neural network-based CO2 interpretation from 4d Sleipner seismic images. J. Geophys. Res.: Solid Earth 126 (12). https://doi.org/10.1029/2021JB022524.

Li, D., Peng, S., Guo, Y., Lu, Y., Cui, X., 2021. CO2 storage monitoring based on time-lapse seismic data via deep learning. Int. J. Greenhouse Gas Control 108, 103336. https://doi.org/10.1016/j.ijggc.2021.103336.

Li, S., Liu, B., Ren, Y., Chen, Y., Yang, S., Wang, Y., Jiang, P., 2020. Deep-learning inversion of seismic data. IEEE Trans. Geosci. Remote Sens. 58 (3), 2135–2149. https://doi.org/10.1109/TGRS.2019.2953473.

Lie, K., Krogstad, S., Ligaarden, I.S., Natvig, J.R., Nilsen, H.M., Skaflestad, B., 2012. Open-source MATLAB implementation of consistent discretisations on complex grids. Computat. Geosci. 16 (2), 297–322. https://doi.org/10.1007/s10596-011-9244-4.

Liu, M., Grana, D., 2020. Petrophysical characterization of deep saline aquifers for CO2 storage using ensemble smoother and deep convolutional autoencoder. Adv. Water Resour. 142, 103634 https://doi.org/10.1016/j.advwatres.2020.103634.

Liu, M., Vashisth, D., Grana, D., Mukerji, T., 2023. Joint inversion of geophysical data for geologic carbon sequestration monitoring: a differentiable physics-informed neural network model. J. Geophys. Res.: Solid Earth 128 (3), e2022JB025372. https://doi.org/10.1029/2022JB025372.

Lumley, D., 2010. 4D seismic monitoring of CO2 sequestration. Lead. Edge 29 (2), 150–155. https://doi.org/10.1190/1.3304817.

Lumley, D., Adams, D., Wright, R., Markus, D., Cole, S., 2008. Seismic monitoring of CO 2 geo-sequestration: realistic capabilities and limitations. In: SEG Technical Program Expanded Abstracts 2008, pp. 2841–2845. https://doi.org/10.1190/1.3063935.

Lüth, S., Bergmann, P., Cosma, C., Enescu, N., Giese, R., Götz, J., Ivanova, A., Juhlin, C., Kashubin, A., Yang, C., Zhang, F., 2011. Time-lapse seismic surface and down-hole measurements for monitoring CO2 storage in the CO2SINK project (Ketzin, Germany). Energy Procedia 4, 3435–3442. https://doi.org/10.1016/j.egypro.2011.02.268.

Mavko, G., Mukerji, T., Dvorkin, J., 2009. The Rock Physics Handbook: Tools for Seismic Analysis of Porous Media, 2nd ed. Cambridge University Press.

Meadows, M., 2008. Time-lapse seismic modeling and inversion of CO2 saturation for storage and enhanced oil recovery. Lead. Edge 27 (4), 506–516. https://doi.org/10.1190/1.2907183.

Nur, A., Wang, Z., 1989. Seismic and Acoustic Velocities in Reservoir Rocks, 1. SEG Geophysics Reprint Series.

Pride, S.R., 2005. In: Rubin, Y., Hubbard, S.S. (Eds.), Hydrogeophysics, 50. Springer Netherlands, pp. 253–290. https://doi.org/10.1007/1-4020-3102-5_9.

Pruess, K., 1991. TOUGH2 Unsaturated Groundwater and Heat Transport Model. Lawrence Berkeley Lab, United States. https://www.osti.gov/biblio/10164618.

Reuss, A., 1929. Calculation of the flow limits of mixed crystals on the basis of the plasticity of monocrystals. ZAMM - Zeitschrift für Angewandte Mathematik und Mechanik 9, 49–58. https://doi.org/10.1002/zamm.19290090104.

Roche, B., Bull, J.M., Marin-Moreno, H., Leighton, T.G., Falcon-Suarez, I.H., Tholen, M., White, P.R., Provenzano, G., Lichtschlag, A., Li, J., Faggetter, M., 2021. Time-lapse imaging of CO2 migration within near-surface sediments during a controlled sub-seabed release experiment. Int. J. Greenhouse Gas Control 109, 103363. https://doi.org/10.1016/j.ijggc.2021.103363.

Ronneberger, O., Fischer, P., Brox, T., 2015. U-net: convolutional networks for biomedicalimage segmentationNavab, N., Hornegger, J., Wells, W.M., Frangi, A.F. (Eds.), In: Medical ImageComputing and Computer-Assisted Intervention – MICCAI 2015, Vol. 9351. Springer International Publishing, pp. 234–241. https://doi.org/10.1007/978-3-319-24574-4_28.

Sinha, S., De Lima, R.P., Lin, Y., Sun, A.Y., Symons, N., Pawar, R., Guthrie, G., 2020. Normal or abnormal? Machine learning for the leakage detection in carbon sequestration projects using pressure field data. Int. J. Greenhouse Gas Control 103, 103189. https://doi.org/10.1016/j.ijggc.2020.103189.

Smit, B., Reimer, J.A., Oldenburg, C.M., Bourg, I.C., 2014. Introduction to Carbon Capture and Sequestration (Vol. 1). Imperial College Press. https://doi.org/10.1142/p911.

Steeples, D.W., 2005. In: Rubin, Y., Hubbard, S.S. (Eds.), Hydrogeophysics, 50. Springer Netherlands, pp. 215–251. https://doi.org/10.1007/1-4020-3102-5_8.

Sun, J., Niu, Z., Innanen, K.A., Li, J., Trad, D.O., 2020. A theory-guided deep-learning formulation and optimization of seismic waveform inversion. Geophysics 85 (2), R87–R99. https://doi.org/10.1190/geo2019-0138.1.

Um, E.S., Alumbaugh, D., Lin, Y., Feng, S., 2022. Real-time deep-learning inversion of seismic full waveform data for CO 2 saturation and uncertainty in geological carbon storage monitoring. Geophys. Prospect. 1365–2478. https://doi.org/10.1111/1365-2478.13197, 13197.

Van der Meer, L.G.H., Arts, R.J., Paterson, L., 2000. Prediction of migration of CO2 after injection in a saline aquifer: reservoir history matching of a 4D seismic image with a compositional gas-water model. In: Proceedings 5th International Conference on Greenhouse Gas Control Technologies, pp. 378–384.

Voigt, W., 1928. Textbook of Crystal Physics. BB Teubner.

Wang, Z., Dilmore, R.M., Harbert, W., 2020. Inferring CO2 saturation from synthetic surface seismic and downhole monitoring data using machine learning for leakage detection at CO2 sequestration sites. Int. J. Greenhouse Gas Control 100, 103115. https://doi.org/10.1016/j.ijggc.2020.103115.

Wen, G., Tang, M., Benson, S.M., 2021. Towards a predictor for CO2 plume migration using deep neural networks. Int. J. Greenhouse Gas Control 105, 103223. https://doi.org/10.1016/j.ijggc.2020.103223.

Wen, G., Li, Z., Azizzadenesheli, K., Anandkumar, A., Benson, S.M., 2022. U-FNO—an enhanced Fourier neural operator-based deep-learning model for multiphase flow. Adv. Water Resour. 163, 104180 https://doi.org/10.1016/j.advwatres.2022.104180.

White, D., 2013. Seismic characterization and time-lapse imaging during seven years of CO2 flood in the Weyburn field, Saskatchewan, Canada. Int. J. Greenhouse Gas Control 16, S78–S94. https://doi.org/10.1016/j.ijggc.2013.02.006.

White, J.E., 1975. Computed seismic speeds and attenuation in rocks with partial gas saturation. Geophysics 40 (2), 224–232. https://doi.org/10.1190/1.1440520.

Wood, A.B., Lindsay, R.B., 1956. A textbook of sound. Phys. Today 9 (11), 37. https://doi.org/10.1063/1.3059819. –37.

Wu, Y., Lin, Y., 2020. Inversionnet: an efficient and accurate data-driven full waveform inversion. IEEE Trans. Comput. Imaging 6, 419–433. https://doi.org/10.1109/TCI.2019.2956866.

Xing, G., Zhu, T., 2019. Modeling frequency-independent q viscoacoustic wave propagation in heterogeneous media. J. Geophys. Res.: Solid Earth 124 (11), 11568–11584. https://doi.org/10.1029/2019JB017985.

Xiong, F., Ba, J., Gei, D., Carcione, J.M., 2021. Data-driven design of wave-propagation models for shale-oil reservoirs based on machine learning. J. Geophys. Res.: Solid Earth 126 (12). https://doi.org/10.1029/2021JB022665.

Xue, Z., Kim, J., Mito, S., Kitamura, K., Matsuoka, T., 2009. Detecting and monitoring co2 with p-wave velocity and resistivity from both laboratory and field scales. In: SPE International Conference on CO2 Capture, Storage, and Utilization. https://doi.org/10.2118/126885-MS. SPE-126885-MS.

Yang, Y., Gao, A.F., Azizzadenesheli, K., Clayton, R.W., Ross, Z.E., 2023. Rapid seismic waveform modeling and inversion with neural operators. IEEE Trans. Geosci. Remote Sens. 61, 1–12. https://doi.org/10.1109/TGRS.2023.3264210.

Yin, Z., Orozco, R., Louboutin, M., Herrmann, F.J., 2023. Solving multiphysics-based inverse problems with learned surrogates and constraints. Adv. Model. Simul. Eng. Sci. 10 (1), 14. https://doi.org/10.1186/s40323-023-00252-0.

Yu, S., Ma, J., 2021. Deep learning for geophysics: current and future trends. Rev. Geophys. 59 (3) https://doi.org/10.1029/2021RG000742.

Zhong, Z., Sun, A.Y., Jeong, H., 2019. Predicting CO2 plume migration in heterogeneous formations using conditional deep convolutional generative adversarial network. Water Resour. Res. 55 (7), 5830–5851. https://doi.org/10.1029/2018WR024592.

Zhong, Z., Sun, A.Y., Wu, X., 2020. Inversion of time-lapse seismic reservoir monitoring data using cyclegan: a deep learning-based approach for estimating dynamic reservoir property changes. J. Geophys. Res.: Solid Earth 125 (3). https://doi.org/10.1029/2019JB018408.

Zhou, Z., Lin, Y., Zhang, Z., Wu, Y., Wang, Z., Dilmore, R., Guthrie, G., 2019. A data-driven CO2 leakage detection using seismic data and spatial–temporal densely connected convolutional neural networks. Int. J. Greenhouse Gas Control 90, 102790. https://doi.org/10.1016/j.ijggc.2019.102790.

Zhu, T., Ajo-Franklin, J.B., Daley, T.M., 2017. Spatiotemporal changes of seismic attenuation caused by injected CO 2 at the Frio-II pilot site, Dayton, TX, USA: spatiotemporal seismic attenuation. J. Geophys. Res.: Solid Earth 122 (9), 7156–7171. https://doi.org/10.1002/2017JB014164.

Zhu, T., Ajo-Franklin, J., Daley, T.M., Marone, C., 2019. Dynamics of geologic CO 2 storage and plume motion revealed by seismic coda waves. In: Proceedings of the National Academy of Sciences, 116, pp. 2464–2469. https://doi.org/10.1073/pnas.1810903116.